

# Chapter 19

## TWO-STREAM INSTABILITY

### 19.1 Introduction

An intense particle beam forms a potential well for oppositely charged particles and will therefore trap particles of the opposite charge. These trapped particles can often accumulate to such an extent that they provide a potential well for particles of the original beam. Thus, the secondary beam can oscillate transversely in the potential well of the primary beam and the primary beam can oscillate transversely in the potential well of the secondary beam. This coupled-beam oscillation may grow in amplitude and lead to beam loss eventually. This is called *two-stream instability*. One way to eliminate the accumulation of particles of opposite charge is to leave a gap in the primary beam so that the secondary particles can be cleared. However, sometimes the accumulation of secondary particles produced by one single passage of the primary beam can be so intense that instability develop even before the clearing gap is reached.

### 19.2 Trapped Electrons

Proton beam trapping electrons was first observed in the Bevatron [1] and later in the CERN Intersecting Storage Ring (ISR) [2]. The ISR was a collider with an intense coasting proton beam in each of the intersecting vacuum chambers. It had been observed that electrons were trapped in the potential of the proton beams with oscillation frequency

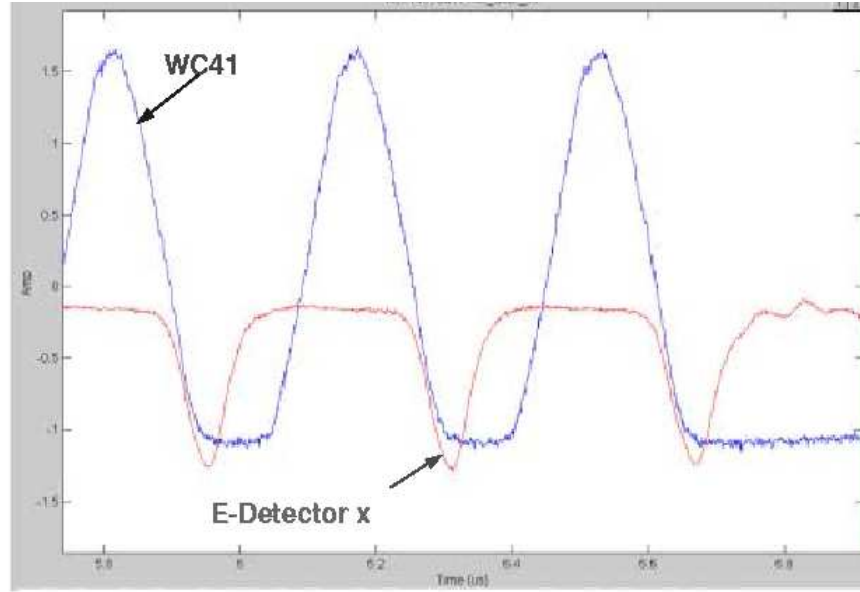


Figure 19.1: (color) Turn-by-turn electron signals are shown in relation to the proton beam pulse at PSR. Electrons start to appear at the back end of the beam pulse and are cleared in the bunch gap.

around 100 MHz. The instability was intermittent. It stopped when the electrons, driven to large amplitudes, were shaken out to the walls, or out of resonance with the protons. It restarted when a sufficient number of new electrons had been accumulated. Slow beam blowup and background problems were the result.

The Proton Storage Ring (PSR) at Los Alamos (LANL) running with  $2.3$  to  $4.2 \times 10^{13}$  protons has always been troubled by the electrons trapped inside the proton beam [3].

A turn-by-turn picture of the electron signal in relation to the circulating proton beam pulse at the end of a 500 ms store is shown in Fig. 19.1. The proton beam has a full width of about 240 ns. The timing between electrons and proton beam is good to a few ns. The electron detector was designed and built at Argonne National Laboratory (ANL). It has a repeller grid, so that it can decouple the electron energy analysis from collection. The repeller voltage of 5 volts means that the electrons have to have a kinetic energy above 5 eV in order to get through to the collector. Electrons start to appear after the peak of the beam pulse has passed and the peak of the electrons appears at the end of the beam pulse. Higher repeller voltage shows a smaller, and narrower pulse. The electron flux hitting the wall is sizeable, about 25 mA/cm<sup>2</sup> at the peak or about 2 pC/cm<sup>2</sup>/pulse or 60 pC/cm/pulse integrated over the circumference of the beam pipe.

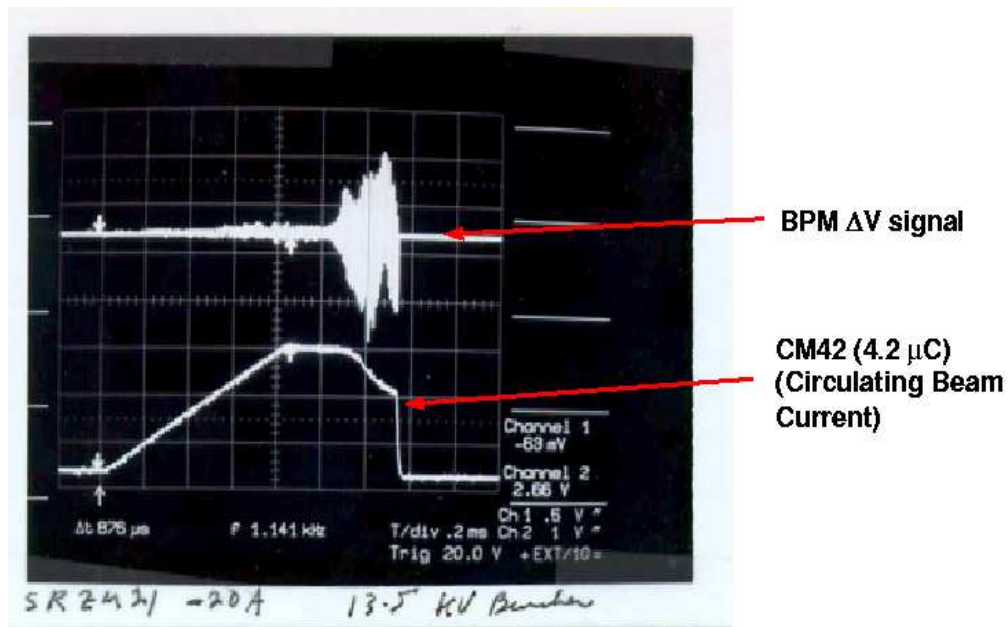


Figure 19.2: (color) Top trace: vertical difference signals of the beam reveal a growing instability about 300  $\mu s$  after the end of injection. Lower trace: sum signals of the beam showing beam loss as the instability grows.

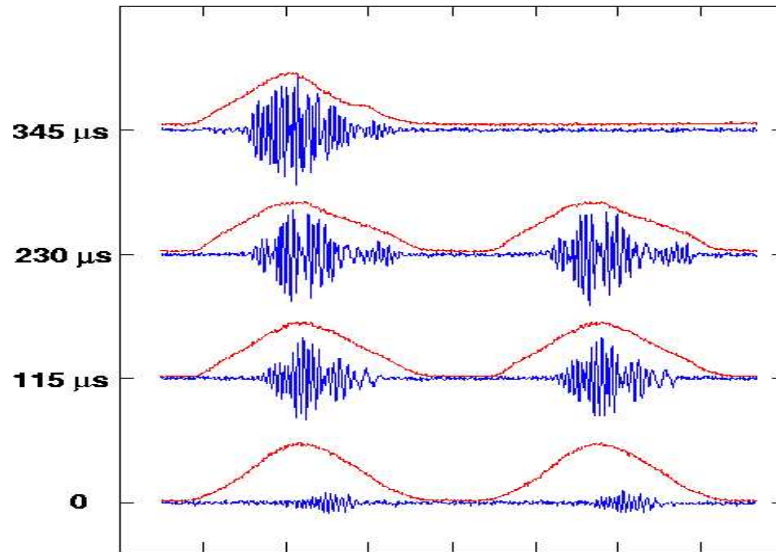


Figure 19.3: (color) Turn-by-turn vertical difference signals from a short stripline beam-position monitor at the final 300  $\mu s$  of the store show a vertical instability starting at the back end of the bunch and spreading into the whole bunch with increasing amplitude. The bunch sum profiles from a wall current monitor are also shown revealing a beam loss as the instability develops.

It is interesting to compare this with the 420 pC/cm average line density of the proton beam. Unfortunately, one cannot deduce from this one picture alone how much electron multi-pactoring is occurring on the backside of the beam pulse without additional data and assumptions.

An instability is clearly seen in Fig. 19.2 when beam is stored for about 300 microseconds after the end of injection. A rapidly growing vertical difference signal (top trace) can be seen shortly before beam loss occurs (lower trace), indicating beam centroid oscillations. In Fig. 19.3, the growth of the instability can be seen turn by turn at the final  $\sim 300 \mu\text{s}$  of the store. Here the vertical difference signal is compared to the wall current monitor trace. The beam transverse instability starts on the backside of the pulse and broadens out as it grows in strength. Some beam loss is evident at the last turn before extraction.

The Brookhaven booster running in the coasting beam mode suffers sudden beam loss due to a vertical instability [4], which cannot be identified with any reasonable amount of transverse impedance. This has been considered to be the result of two-stream instability between the proton beam and the electrons it traps.

The Fermilab antiproton ring traps positive ions and limits the intensity of the storage [5]. The newly built Advanced Photon Source (APS) at ANL is a synchrotron light source using a positron beam. It has been observed that electrons are trapped causing instability [6].

### 19.2.1 Single-Electron Mechanics

Coupled-centroid oscillation of the proton beam and the trapped electron beam will occur only when the amount of electrons becomes very intense. Therefore, to prevent such instability, we would like the electrons in the vacuum chamber not to accumulate. The electrons inside the vacuum chamber are supposed not to move longitudinally. As the proton bunch passes through them, they are attracted towards the central axis of the proton bunch with vertical electron *bounce frequency*  $\Omega_e/(2\pi)$  given by [12]

$$\Omega_e^2 = \frac{4N_p r_e c^2}{a_v(a_v + a_H)L_b} . \quad (19.1)$$

Here,  $N_p$  is the number of protons in the bunch which has an elliptical cross section with vertical and horizontal radii  $a_v$  and  $a_H$ ,  $L_b$  is the full bunch length, and  $r_e$  the

electron classical radius. In our derivation, we assume that the proton beam has uniform longitudinal and transverse distributions and has a cylindrical cross section with radius  $a$  inside a cylindrical beam pipe of radius  $b$ . Thus  $a_v(a_v + a_H)$  can be replaced by  $2a^2$ . The images of the proton beam and the electron cloud in the walls of the vacuum chamber will modify the electron bounce frequency depicted in Eq. (19.1), but their effects are neglected in this study. Only linear focusing force acting on the electrons by the proton beam will be considered. The bounce frequency in Eq. (19.1) can be derived exactly as the space charge self-force tune shift in Chapter 4. In Eq. (4.24), for example, we make the replacement  $2\nu_0^{V,H}\Delta\nu_0^{V,H}\omega_0^2 \rightarrow \Omega_e^2$  and  $2a^2 \rightarrow a_v(a_v + a_H)$ . We delete one factor of  $\gamma$  from the denominator because the trapped electrons are assumed to have no longitudinal motion. We delete the other factor of  $\gamma^2$  from the denominator because the trapped electrons, having no longitudinal velocity, do not interact with the magnetic field of the proton beam.

An electron trapped inside the proton beam performs betatron oscillations with an equivalent betatron function\*  $\beta_b = \beta c/\Omega_e$  with a total betatron phase advance  $\phi_b = \Omega_e L_b/v$ , where  $\beta c$  is the velocity of the protons. After the passage of the proton bunch, the motion of the electron in the gap is equivalent to a drift of length  $L_g = \lambda_{rf} - L_b$  with  $\lambda_{rf}$  being the rf wavelength or width of the stationary bucket. Here, we assume all rf buckets are filled. The transfer matrix for an rf wavelength is [7]

$$M = \begin{pmatrix} 1 & L_g \\ 0 & 1 \end{pmatrix} \begin{pmatrix} \cos \phi_b & \beta_b \sin \phi_b \\ -\frac{1}{\beta_b} \sin \phi_b & \cos \phi_b \end{pmatrix} = \begin{pmatrix} \cos \phi_b - \frac{L_g}{\beta_b} \sin \phi_b & \beta_b \sin \phi_b + L_g \cos \phi_b \\ -\frac{1}{\beta_b} \sin \phi_b & \cos \phi_b \end{pmatrix}. \quad (19.2)$$

In order that the electron will not be trapped inside the proton bunch, its motion has to be unstable or

$$\frac{1}{2}|\text{Tr}M| = \left| \cos \phi_b - \frac{L_g}{2\beta_b} \sin \phi_b \right| > 1. \quad (19.3)$$

If the electron is unstable, we can write

$$\frac{1}{2}|\text{Tr}M| = \cosh \mu, \quad (19.4)$$

where  $\mu^{-1}$  is the growth of the electron oscillation amplitude in one rf bucket, and the growth rate is  $\mu\beta c/\lambda_{rf}$ . Here, we study the effect of trapped electrons in three

---

\*The electron bounce tune is  $Q_e\Omega_e/\omega_0$  and the equivalent betatron function is  $\beta_b = R/Q_e$ , where  $R$  is the mean radius of the accelerator ring.

synchrotron rings: the storage ring of the Spallation Neutron Source (SNS) to be built at Oak Ridge National Laboratory (ORNL), the Los Alamos PSR, and the booster at Brookhaven (BNL). Some information of the three rings are listed in Table 19.1.

Table 19.1: Some data of the Oak Ridge SNS, the Los Alamos PSR, and the Brookhaven booster at injection.

	Oak Ridge SNS	Los Alamos PSR	Brookhaven Booster
Circumference $C$ (m)	220.6880	90.2000	201.769
Injection kinetic energy (GeV)	1.000	0.797	0.200
$\gamma$	2.0658	1.8494	1.2132
$\beta$	0.8750	0.8412	0.5662
Revolution frequency $f_0$ (MHz)	1.1887	2.7959	0.8412
Revolution period $T_0$ (ns)	841.3	357.7	1189
Total number of protons $N_p$	$2.1 \times 10^{14}$	$4.2 \times 10^{13}$	$2.4 \times 10^{13}$
Rf harmonic (no. of bunches) $h$	1	1	1
Number of injection turns	1225	2000	300
Repetition rate (Hz)	60	12	7.5

Equation (19.3) appears to be a simple criterion. In fact, it is much more complex in application, because the electron bounce frequency turns out to be usually very high. Take for example the PSR, we find  $\Omega_e = 1.254$  GHz, which gives an equivalent betatron function  $\beta_b = \beta_c/\Omega_e = 0.201$  m. With the gap length 30.07 m,  $L_g/\beta_b = 150$ . Although  $\Omega_e$  is not sensitive to  $L_g/\beta_b$ , it is very sensitive to the phase  $\phi_b = \Omega_e L_g/v \approx 299$  rad and therefore to  $\sin \phi_b$  and  $\cos \phi_b$ . Thus, a very slight change in the number of protons in the beam will alter the electron bounce frequency, the betatron phase, and give rise to a large change in the trace. Since the electron bounce frequency usually has a large spread, it is more reasonable to consider the rms value of the trace instead.

The results of  $\frac{1}{2}|\text{Tr}M|$  are listed in Table 19.2. We see that for all the 3 rings, the electrons trapped should be able to escape to the walls of the beam pipe in the beam gap. In fact, with such high electron bounce frequency,  $L_g/\beta_b$  will be large and it will not be easy to trap electrons if the gap is clean. When the intensity of the proton beam is raised, the electron bounce frequency will increase, making the electrons easier to escape at the gap.

Table 19.2: Instability and escape time through the bunch gap of a single electron trapped inside the proton bunches of the ORNL SNS, LANL PSR, and BNL booster.

	Oak Ridge SNS	Los Alamos PSR	Brookhaven Booster
Injection full bunch length (m)	143.39	60.13	100.89
Gap length (m)	77.30	30.07	100.89
Proton beam radius $a$ (m)	0.0380	0.0150	0.0150
Bounce angular frequency $\Omega_e$ (MHz)	713.3	1253.9	462.6
Bounce betatron phase $\phi_b$ (rad)	309.9	299.0	435.2
$\frac{1}{2} \text{Tr}M $ (rms)	52.55	37.38	108.8
Escape time in no. of rf buckets	0.2148	0.2318	0.1858

Sometimes, the gap is not totally free of protons. The space charge effect of the protons will distort the rf bucket reducing its momentum acceptance. As a result, some protons may leak out of the bucket and end up in the bunch gap. If a fraction  $\eta$  of the protons leaks into the gap, the electron will oscillate with bounce frequency  $\Omega_{eb}/(2\pi)$  inside the proton beam and bounce frequency  $\Omega_{eg}/(2\pi)$  in the bunch gap. These frequencies are given by [7, 10]

$$\Omega_{eb}^2 = \Omega_e^2(1 - \eta) \quad \text{and} \quad \Omega_{eg}^2 = \Omega_e^2 \eta \frac{L_b}{L_g}. \quad (19.5)$$

Again, only linear focusing force by the proton beam is considered. The betatron phase advances in the beam and in the gap are, respectively,  $\phi_b = \Omega_{eb}L_b/(\beta c)$  and  $\phi_g = \Omega_{eg}L_g/(\beta c)$ . The transfer matrix is therefore

$$\begin{aligned}
 M &= \begin{pmatrix} \cos \phi_g & \beta_g \sin \phi_g \\ -\frac{1}{\beta_g} \sin \phi_g & \cos \phi_g \end{pmatrix} \begin{pmatrix} \cos \phi_b & \beta_b \sin \phi_b \\ -\frac{1}{\beta_b} \sin \phi_b & \cos \phi_b \end{pmatrix} \\
 &= \begin{pmatrix} \cos \phi_g \cos \phi_b - \frac{\beta_g}{\beta_b} \sin \phi_g \sin \phi_b & \beta_b \cos \phi_g \sin \phi_b + \beta_g \cos \phi_b \sin \phi_g \\ -\frac{1}{\beta_g} \cos \phi_b \sin \phi_g - \frac{1}{\beta_b} \cos \phi_g \sin \phi_b & -\frac{\beta_b}{\beta_g} \sin \phi_b \sin \phi_g + \cos \phi_g \cos \phi_b \end{pmatrix}, \quad (19.6)
 \end{aligned}$$

where the equivalent betatron functions in the bunch and in the gap are, respectively,

$$\beta_b = \frac{\beta c}{\Omega_{eb}} \quad \text{and} \quad \beta_g = \frac{\beta c}{\Omega_{eg}}. \quad (19.7)$$

The condition for the electrons to escape is therefore

$$\frac{1}{2}|\text{Tr}M| = \left| \cos \phi_g \cos \phi_b - \frac{1}{2} \left( \frac{\Omega_{eb}}{\Omega_{eg}} + \frac{\Omega_{eg}}{\Omega_{eb}} \right) \sin \phi_g \sin \phi_b \right| > 1 . \quad (19.8)$$

It is easy to demonstrate that Eq. (19.8) reduces to Eq. (19.3) when  $\eta \rightarrow 0$ .

Figure 19.4 show  $\frac{1}{2}\text{Tr}M$  as a function of the fractional proton leakage  $\eta$  into the gap, respectively, for the ORNL SNS, LANL PSR, and BNL booster. The plots for the ORNL SNS and LANL PSR are very similar;  $\frac{1}{2}\text{Tr}M$  oscillates rapidly with the fractional leakage and becomes bounded by  $\pm 1$  or electrons will be trapped when  $\eta \lesssim 0.05$ . The situation for the BNL booster is different. Even up to  $\eta = 0.20$ , the oscillation of  $\frac{1}{2}\text{Tr}M$  still has an amplitude larger than 1. This is mainly due to the fact of a larger gap-to-bunch-length ratio in the BNL booster. Thus, we may conclude that electrons are not so easily trapped in BNL booster as in the ORNL SNS and LANL PSR when protons are spilled into the bunch gaps. We also try to vary the electron bounce frequency in each case and find that the results remain relatively the same. The only changes in the plots are faster oscillations when the bounce frequency is increased.

### 19.2.2 Centroid-Oscillation Instability

Consider coupled oscillation of the proton beam and the electron ‘beam’ in the vertical direction. The displacements of a proton and electron from the central axis of the vacuum chamber are denoted, respectively, by  $y_p$  and  $y_e$ . Here, we assume both the proton and electron beams are coasting beams having the same transverse sizes and uniform distribution longitudinally and transversely. The coupled equations of motion are [12, 7, 4, 14]

$$\left( \frac{\partial}{\partial t} + \omega_0 \frac{\partial}{\partial \theta} \right)^2 y_p + Q_\beta^2 \omega_0^2 y_p = -Q_p^2 \omega_0^2 (y_p - \bar{y}_e) + Q_{ps}^2 \omega_0^2 (y_p - \bar{y}_p) , \quad (19.9)$$

$$\frac{d^2 y_e}{dt^2} = -Q_e^2 \omega_0^2 (y_e - \bar{y}_p) + Q_{es}^2 \omega_0^2 (y_e - \bar{y}_e) , \quad (19.10)$$

where  $\bar{y}_p$  and  $\bar{y}_e$  are the vertical displacements of the centroids of, respectively, the proton and electron beams from the axis of the vacuum chamber,  $\omega_0$  is the angular revolution frequency,  $\theta$  is the azimuthal angle around the ring,  $Q_\beta$  is the betatron tune, and  $Q_p$  and  $Q_e$  are, respectively, the oscillation tune of the electrons inside the proton beam and



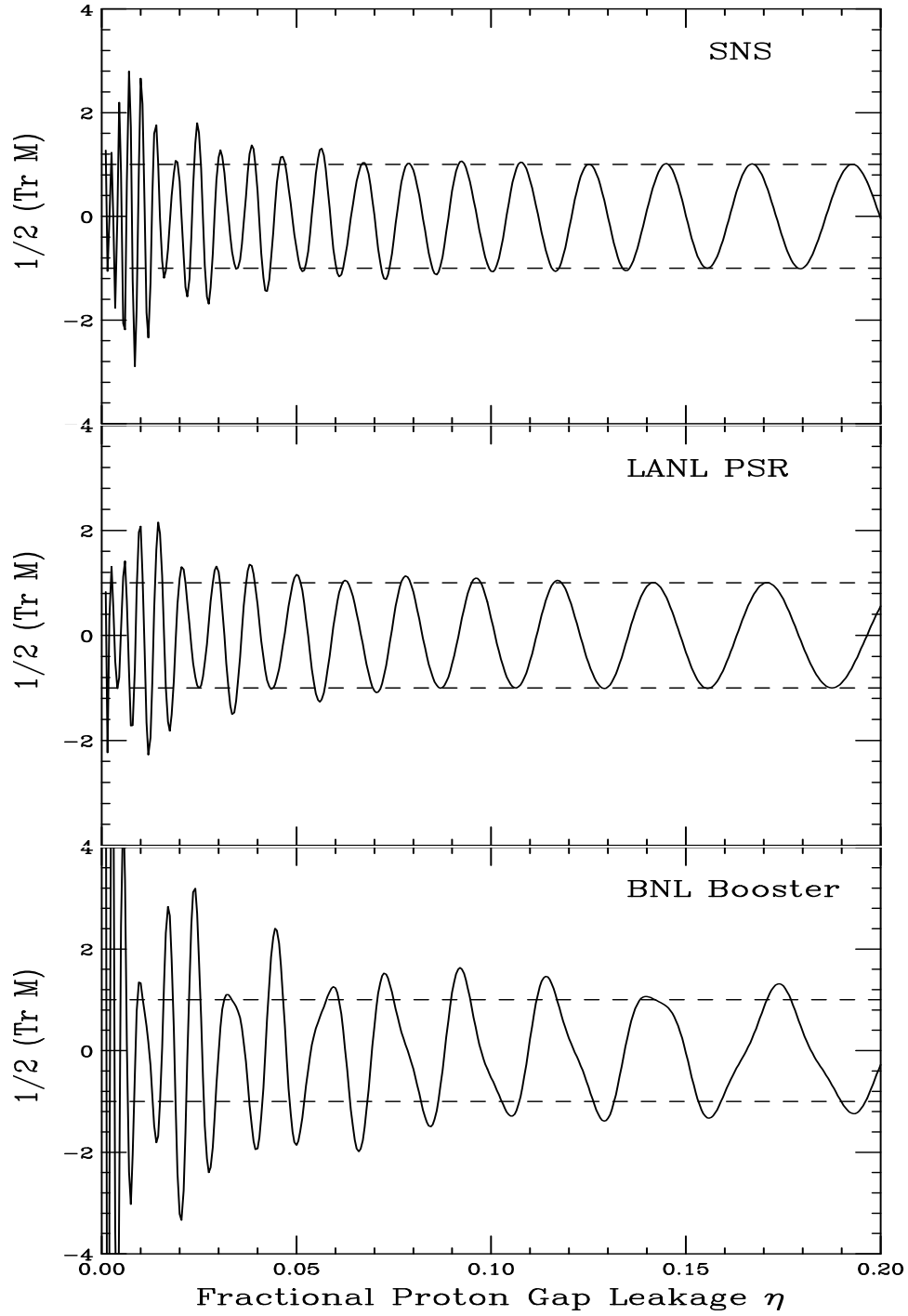


Figure 19.4: The ORNL SNS: Electrons will be trapped if  $\frac{1}{2}\text{Tr}M$  falls between the  $\pm 1$  dashed lines. The 3 plots are, from top down, for the ORNL SNS, LANL PSR, and BNL booster.

the oscillation tune of the protons inside the electron beam. We have

$$\Omega_e^2 = (Q_e \omega_0)^2 = \frac{4N_p r_e c^2}{a_v(a_H + a_v)C} , \quad (19.11)$$

$$\Omega_p^2 = (Q_p \omega_0)^2 = \frac{4N_p r_p c^2 \chi_e}{a_v(a_H + a_v)\gamma C} , \quad (19.12)$$

where  $\chi_e$  is the neutralization factor, or the ratio of the electron distribution to the proton distribution. In above,  $r_p$  is the classical proton radius,  $r_e$  the classical electron radius, and  $C$  the circumference of the accelerator ring. The negative signs on first terms on the right hand sides of Eqs. (19.9) and (19.10) indicate that the protons are focused by the electron beam and the electrons are focused by the proton beam. The factor  $\gamma$  in the denominator of  $\Omega_p^2$  comes about because the protons are circulating around the ring while the electrons do not. Notice that there are no magnetic force contributions. For  $\Omega_e$ , the electron has no velocity although it sees a magnetic field from the proton beam. For  $\Omega_p$ , the proton, although at a high velocity, does not see a magnetic field in the stationary electron beam. Again, we are considering uniformly and cylindrical-symmetrically distributed proton and electron beams of radius  $a$ ; or  $a_v(a_H + a_v) \rightarrow 2a^2$ . Image effects in the walls of the vacuum chamber as well as nonlinear focusing forces are neglected.

The last term in the proton equation denotes the oscillations of the proton under the self-field of the proton beam. Here,

$$(Q_{ps} \omega_0)^2 = \frac{4N_p r_p c^2}{a_v(a_H + a_v)\gamma^3 C} \quad (19.13)$$

is proportional to the linear space charge tune shift of the proton beam. Similarly the last term in the electron equation, with

$$Q_{es}^2 = Q_e^2 \chi_e \quad (19.14)$$

denoting the space charge tune shift of the electron beam, depicts the corresponding oscillations of the electron in the self-field of the electron beam.

Averaging over the proton displacements and electron displacements, we obtain the equations for the coupled motion of the proton-beam centroid  $\bar{y}_p$  and the electron-beam centroid  $\bar{y}_e$ . Notice that the space charge terms,  $Q_{ps}^2$  and  $Q_{es}^2$ , drop out. If there is a coherent instability occurring at the angular frequency  $\Omega = Q\omega_0$ , we can write

$$\bar{y}_p \sim e^{i(n\theta - \Omega t)} \quad \text{and} \quad \bar{y}_e \sim e^{i(n\theta - \Omega t)} , \quad (19.15)$$

where  $n$  is the longitudinal harmonic number. The coupled equations can be readily solved to give

$$(Q^2 - Q_e^2)[(n - Q)^2 - Q_\beta^2 - Q_p^2] - Q_e^2 Q_p^2 = 0 , \quad (19.16)$$

which is a quartic. For a solution when  $Q$  is near  $Q_e$ , we can expand  $Q$  around  $Q_e$ . When  $Q_p$  or the neutralization factor  $\chi_e$  is large enough, the solution becomes complex and an instability occurs. The limiting  $Q_p$  for stability is given by

$$Q_p \lesssim \frac{|(n - Q_e)^2 - Q_\beta^2 - Q_p^2|}{2\sqrt{Q_e|n - Q_e|}} , \quad (19.17)$$

from which the limiting neutralization factor  $\chi_e$  can be obtained. Once above threshold, the growth rate, given by

$$\frac{1}{\tau} \approx \frac{Q_p \omega_0}{2} \sqrt{\frac{Q_e}{|n - Q_e|}} , \quad (19.18)$$

is very fast. Notice that  $Q_p^2$  on the right side of Eq. (19.17) in the numerator can be neglected because usually  $Q_p^2 \ll Q_\beta^2$ .

A proper employment of Eq. (19.17) is important, because it can give meaningless result. For example, in the situation:

$$[Q_e] = [Q_\beta] \quad \text{or} \quad [Q_e] + [Q_\beta] = 1 , \quad (19.19)$$

where  $[Q_e]$  and  $[Q_\beta]$  are, respectively, the residual betatron tune and the residual electron bounce tune, there will always exist a harmonic  $n$  which leads to instability for  $Q_p \rightarrow 0$  or neutralization  $\chi_e \rightarrow 0$ . However, the growth rate will go to zero also. In reality, there is always a variation in the proton linear density or the electron bounce tune  $Q_e$  usually has a spread. Furthermore, the betatron tune can be suitably adjusted. To obtain something meaningful, first let us separate the numerator of the right side of Eq. (19.17) into the fast and slow waves and keep only the dangerous slow wave:

$$|(n - Q_e)^2 - Q_\beta^2 - Q_p^2| \approx 2Q_\beta|n - Q_e - Q_\beta| \quad (19.20)$$

Compute  $Q_e$  from Eq. (19.11). Then the most offending harmonic  $n$  is determined as the integer closest to  $Q_e + Q_\beta$ . We next modify  $Q_e$  slightly so that

$$n - Q_e - Q_\beta = \frac{1}{2} . \quad (19.21)$$

Table 19.3: Coherent centroid-oscillation instability for proton-electron coasting beams.

	Oak Ridge	Los Alamos	Brookhaven
	SNS	PSR	Booster
Total number of protons $N_p$	$2.10 \times 10^{14}$	$4.2 \times 10^{13}$	$4.42 \times 10^{13}$
Betatron tune $Q_\beta$	5.82	2.14	4.80
Proton beam radius $a$ (m)	0.0380	0.0150	0.0150
$Q_p/\sqrt{\chi_e}$	1.2501	1.000	1.070
Most offending harmonic $n$	83	61	67
$Q_e = n - Q_\beta - \frac{1}{2}$	76.68	58.36	79.70
Limiting $Q_p$	0.1378	0.0957	0.1227
Limiting neutralization $\chi_e$	0.0122	0.0093	0.0132
Growth rate in number of turns	0.637	0.637	0.637
Landau damping with $(\Delta Q_\beta - 2\Delta Q_{sc})/Q_\beta = 0.03$ and $\Delta Q_e/Q_e - \chi_e = 0.25$			
Limiting $Q_p$	0.5040	0.1853	0.4157
Limiting neutralization $\chi_e$	0.1626	0.0343	0.151
Growth rate in number of turns	0.176	0.340	0.386

As a result, the stability condition of Eq. (19.17) reduces to

$$Q_p \lesssim \frac{1}{2} \sqrt{\frac{Q_\beta}{Q_e}}, \quad (19.22)$$

and the growth rate of Eq. (19.18) reduces to

$$\frac{1}{\tau} \approx \frac{Q_p \omega_0}{2} \sqrt{\frac{Q_e}{Q_\beta}}. \quad (19.23)$$

The latter becomes  $\tau^{-1} \approx \omega_0/4$  when the threshold values in Eq. (19.22) are substituted.

With this consideration, the results are listed in Table 19.3. Here, the intensity of  $4.42 \times 10^{13}$  protons is used for the Brookhaven booster, where coasting beam experiments with possible e-p instabilities have been observed. We notice that the neutralization threshold is about 1.2% for the ORNL SNS, 0.9% for the LANL PSR, and 1.3% for the BNL booster. Once the thresholds are reached, the growth rates are very fast and the corresponding growth times are less than one turn for all the 4 machines.

There is another consideration of the stability of the two beam centroids, since the coherent oscillation can be stabilized by Landau damping. The equation of motion of the electron, Eq. (19.10), can be viewed as an undamped oscillator driven by  $\bar{y}_p$ , the centroid of the proton beam. Thus, spreads in the proton betatron tune  $Q_\beta$  and/or proton bounce tune  $Q_p$  alone will not be able to damp the electron oscillations. To damp the electron oscillation, there must be a spread in the electron bounce tune  $Q_e$ . The same applies to the equation of motion of the proton, Eq. (19.9), driven by the centroid of the electron beam. Therefore, to provide Landau damping to the coupled-centroid oscillation, there must exist large enough spreads in both the betatron tune  $\Delta Q_\beta$  and the electron bounce tune  $\Delta Q_e$ .

First, we rewrite Eqs. (19.9) and (19.10) as

$$\left( \frac{\partial}{\partial t} + \dot{\theta} \frac{\partial}{\partial \theta} \right)^2 y_p + Q_p'^2 \omega_0^2 y_p = Q_p^2 \omega_0^2 \bar{y}_e - Q_{ps}^2 \omega_0^2 \bar{y}_p, \quad (19.24)$$

$$\frac{d^2 y_e}{dt^2} + Q_e'^2 \omega_0^2 y_e = Q_e^2 \omega_0^2 \bar{y}_p - Q_{es}^2 \omega_0^2 \bar{y}_e, \quad (19.25)$$

where we have denoted

$$Q_p'^2 = Q_\beta^2 + Q_p^2 - Q_{ps}^2 \quad \text{and} \quad Q_e'^2 = Q_e^2 - Q_{es}^2. \quad (19.26)$$

Second, with the ansatz in Eq. (19.15), the coupled differential equations becomes

$$y_p = \frac{Q_p^2 \bar{y}_e - Q_{ps}^2 \bar{y}_p}{Q_p'^2 - \left( Q - \frac{n\dot{\theta}}{\omega_0} \right)^2}, \quad (19.27)$$

$$y_e = \frac{Q_e^2 \bar{y}_p - Q_{es}^2 \bar{y}_e}{Q_e'^2 - Q^2}. \quad (19.28)$$

Third, we need to integrate both sides with the suitable distribution functions. In doing so, two approximations are to be made: (1) only the denominators of Eqs. (19.27) and (19.28) depend on the distributions which appear in differences of squares but not the numerator, and (2) only the *slow wave* will be included. It is then easy to obtain

$$\bar{y}_p = \frac{Q_p^2}{2Q_p' \delta Q_p'} \bar{y}_e - \frac{Q_{ps}^2}{2Q_p' \delta Q_p'} \bar{y}_p, \quad (19.29)$$

$$\bar{y}_e = \frac{Q_e^2}{2Q_e' \delta Q_e'} \bar{y}_p - \frac{Q_{es}^2}{2Q_e' \delta Q_e'} \bar{y}_e, \quad (19.30)$$

where

$$\frac{1}{\delta Q'_p} = \int \frac{F_p(s) ds}{Q'_p - n + Q + \delta_p s} , \quad (19.31)$$

$$\frac{1}{\delta Q'_e} = \int \frac{F_e(s) ds}{Q'_e - Q + \delta_e s} , \quad (19.32)$$

$$\delta_p = \frac{\partial}{\partial s} \left( Q'_p(s) - \frac{n\dot{\theta}(s)}{\omega_0} \right)_{s=0} , \quad (19.33)$$

$$\delta_e = \left( \frac{\partial Q'_e(s)}{\partial s} \right)_{s=0} , \quad (19.34)$$

and  $Q_p$ ,  $Q'_p$ ,  $Q_{ps}$ ,  $Q_e$ ,  $Q'_e$ ,  $Q_{es}$  in Eqs. (19.29) to (19.32) are all evaluated at  $s = 0$ . Here,  $s$  being a generic variable, which can represent amplitude, momentum spread, etc, while  $F_p(s)$  and  $F_e(s)$  are distributions normalized to unity for the protons and electrons. From Eqs. (19.29) and (19.30), it is easy to get

$$\left( 2\delta Q'_p + \frac{Q_{ps}^2}{Q'_p} \right) \left( 2\delta Q'_e + \frac{Q_{es}^2}{Q'_e} \right) - \frac{Q_p^2 Q_e^2}{Q'_p Q'_e} = 0 . \quad (19.35)$$

Now following Laslett, *et al*, semi-circular distributions,

$$F_p(s) = \frac{2}{\pi \hat{s}_p^2} \sqrt{\hat{s}_p^2 - s^2} \quad \text{and} \quad F_e(s) = \frac{2}{\pi \hat{s}_e^2} \sqrt{\hat{s}_e^2 - s^2} , \quad (19.36)$$

are assumed for both the protons and electrons. One obtains

$$\begin{cases} 2\delta Q'_p = Q'_p - n + Q + i\bar{\Delta}_p , \\ 2\delta Q'_e = Q'_e - Q - i\bar{\Delta}_e , \end{cases} \quad (19.37)$$

where

$$\begin{cases} \bar{\Delta}_p = \sqrt{\Delta Q_p^2 - (Q - n + Q'_p)^2} , \\ \bar{\Delta}_e = \sqrt{\Delta Q_e^2 - (Q - Q'_e)^2} , \end{cases} \quad (19.38)$$

while  $\Delta Q_p$  and  $\Delta Q_e$  are the actual half spread of  $Q'_p$  and  $Q'_e$  in these distributions and are related to  $\delta_p$  and  $\delta_e$  in Eqs. (19.33) and (19.34) by

$$\Delta Q_p = \hat{s}_p \delta_p = \hat{s}_p \frac{\partial}{\partial s} \left( Q'_p(s) - \frac{n\dot{\theta}(s)}{\omega_0} \right)_{s=0} , \quad (19.39)$$

$$\Delta Q_e = \hat{s}_e \delta_e = \hat{s}_e \left( \frac{\partial Q'_e}{\partial s} \right)_{s=0} . \quad (19.40)$$

Equation (19.35) is obtained via the integral [9]

$$\int_{-1}^1 \frac{\sqrt{1-x^2} dx}{x+x_1-i\epsilon} = \pi \left[ x_1 + i\sqrt{1-x_1^2} \right] . \quad (19.41)$$

Substitution into Eq. (19.35) leads to a quadratic equation in the coherent coupled-oscillation tune  $Q$ , the solution of which is

$$Q = Q'_e + \frac{Q_{es}^2}{Q'_e} + d_1 - \frac{i}{2} (\bar{\Delta}_e + \bar{\Delta}_p) \pm i \left\{ \frac{Q_p^2 Q_e^2}{Q'_p Q'_e} - \left[ d_1 + \frac{i}{2} (\bar{\Delta}_e - \bar{\Delta}_p) \right]^2 \right\}^{1/2} , \quad (19.42)$$

where

$$d_1 = \frac{1}{2} \left[ \left( n - Q'_p - \frac{Q_{ps}^2}{Q'_p} \right) - \left( Q'_e + \frac{Q_{es}^2}{Q'_e} \right) \right] . \quad (19.43)$$

It is clear that stability requires in Eq. (19.42)

$$\Re \left\{ \frac{Q_p^2 Q_e^2}{Q'_p Q'_e} - \left[ d_1 + \frac{i}{2} (\bar{\Delta}_e - \bar{\Delta}_p) \right]^2 \right\}^{1/2} \leq \frac{1}{2} (\bar{\Delta}_e + \bar{\Delta}_p) . \quad (19.44)$$

This criterion is equivalent to, after considerable amount of algebra,

$$\bar{\Delta}_p \bar{\Delta}_e \geq \frac{Q_p^2 Q_e^2}{Q'_p Q'_e} \left[ 1 + \left( \frac{2d_1}{\bar{\Delta}_p + \bar{\Delta}_e} \right)^2 \right]^{-1} . \quad (19.45)$$

Within a narrow band of instability, associated with the resonance  $d_1 \approx 0$ , or  $n - Q'_p - Q \approx Q_{ps}^2/Q'_p$  and  $|Q'_e - Q| \approx Q_{es}^2/Q'_e$ , the stability limit can be simplified. With the substitution of Eq. (19.38), we finally arrive at

$$\left[ \Delta Q_p^2 - \left( \frac{Q_{ps}^2}{Q'_p} \right)^2 \right]^{1/2} \left[ \Delta Q_e^2 - \left( \frac{Q_{es}^2}{Q'_e} \right)^2 \right]^{1/2} \geq \frac{Q_p^2 Q_e^2}{Q'_p Q'_e} . \quad (19.46)$$

Because square roots are involved, we also require

$$\Delta Q_p > \left| \frac{Q_{ps}^2}{Q'_p} \right| \quad \text{and} \quad \Delta Q_e > \left| \frac{Q_{es}^2}{Q'_e} \right| . \quad (19.47)$$

It is important to point out that the space charge self-force terms of Eqs. (19.9) and (19.10) do not drop out when averaged over the distributions. As an approximation,

$Q'_p \sim Q_\beta$  implying that  $Q_{ps}^2/Q'_p \sim 2\Delta Q_{sc}$ , where  $\Delta Q_{sc}$  is the linear space charge tune shift of the proton beam. Similarly, we can write  $Q_{es}^2/Q'_e \sim Q_e\chi_e$ , which is twice the linear space charge tune shift of the electron beam. The stability condition then simplifies to

$$[\Delta Q_\beta^2 - 4\Delta Q_{sc}^2]^{1/2} [\Delta Q_e^2 - \chi_e^2 Q_e^2]^{1/2} \gtrsim \frac{Q_p^2 Q_e}{Q_\beta}. \quad (19.48)$$

Because of the square roots on the left side of Eq. (19.48), we also require for stability,

$$\Delta Q_\beta \geq 2Q_{sc} \quad \text{and} \quad \frac{\Delta Q_e}{Q_e} \geq \chi_e. \quad (19.49)$$

The spread in the electron bounce frequency is difficult to measure. However, when instability occurs, the electron bounce frequency is very close to the coherent instability frequency, which is the same for the proton beam and the electron. Thus measuring the coherent transverse oscillation frequency of the proton beam, we can infer the electron bounce frequency. According to the measurement at PSR,  $\Delta Q_e/Q_e \sim 0.25$ . Assuming that the neutralization factor is small, we may set the half maximum fractional spread of the electron bounce tune to be  $\Delta Q_e/Q_e - \chi_e \sim 0.1$ , and the half maximum fractional spread of the betatron tune in excess of twice the space charge tune shift is  $(\Delta Q_\beta - 2\Delta Q_{sc})/Q_\beta \sim 0.03$ . The limiting  $Q_p$  and neutralization factor  $\chi_e$  can now be computed and are also listed in Table 19.3. For the ORNL SNS and the Brookhaven booster, the threshold neutralization factors have been increased to 16.3% and 15.1%, respectively, which are more than 10 times. For the LANL PSR, however, the neutralization threshold  $\chi_e$  becomes  $\sim 3.4\%$ , an increase of less than 4 times. Further increase in threshold requires larger spreads in  $Q_e$  and  $Q_\beta$ . In fact, it has been demonstrated that anti-damping can even happen unless there is a large enough overlap between  $\Delta Q_\beta$  and  $\Delta Q_e$  [12]. Notice that these stability limits of the neutralization factor can be sensitive to the distributions of the betatron tune and the electron bounce tune.

A stability condition has also been derived by Schnell and Zotter [12] assuming parabolic distributions for the betatron tune and the electron bounce tune, but without consideration of the space charge self-forces. They obtain

$$\frac{\Delta Q_\beta}{Q_\beta} \frac{\Delta Q_e}{Q_e} \gtrsim \frac{9\pi^2}{64} \frac{Q_p^2}{Q_\beta^2}. \quad (19.50)$$

Notice that the Schnell-Zotter criterion is essentially the same as the Laslett-Sessler-Möhl criterion, if we interpret  $\Delta Q_\beta$  of the former as the half tune spread of the betatron tune *in excess* of twice the space charge tune spread of the proton beam, and  $\Delta Q_e$  as



the half tune spread of the electron bounce tune *in excess* of twice the space charge tune spread of the electron beam. The factor  $9\pi^2/64$  in Eq. (19.50) is probably a form factor of the parabolic distributions. Our discussion can be generalized when we notice that both  $Q_{ps}^2/Q'_p$  and  $Q_{es}^2/Q'_e$  in Eq. (19.46) come from, respectively, the  $\bar{y}_e$  term in Eq. (19.9) and the  $\bar{y}_p$  term in Eq. (19.10). Thus,  $Q_{ps}^2$  and  $Q_{es}^2$  can be extended to include the perturbations of oscillations coming from all types of impedances of the accelerator ring. In that case, the Schnell-Zotter stability criterion should be valid if we interpret  $\Delta Q_\beta$  as the half tune spread of the betatron tune in excess of what is necessary to cope with the instabilities of the single proton beam, and  $\Delta Q_e$  as the half tune spread of the electron bounce tune in excess of what is necessary to cope with the instabilities of the single electron beam.

### 19.2.3 Production of Electrons

As seen in the previous section, the e-p coherent centroid-oscillation instability depends strongly on the neutralization factor, or the amount of electrons trapped inside the proton bunch.

One source of electron production is through collision of the protons with the residual gas in the vacuum chamber. At a vacuum pressure of  $1 \times 10^{-7}$  Torr (1 atm = 760 Torr) and room temperature ( $T = 300^\circ\text{K}$ ), there is a residual gas density of

$$n_{\text{res}} = \frac{N_A p}{RT} = 3.2 \times 10^{15} \text{ molecules/m}^3, \quad (19.51)$$

where the ideal gas law has been used, with  $N_A = 6.022 \times 10^{23}$  being the Avogadro number and  $R = 82.55 \times 10^{-6} \text{ Atm-m}^3\text{K}^{-1}$  the gas constant. The expected average ionization cross section is  $\sigma_i = 1.2 \times 10^{-18} \text{ cm}^2$  (or 1.2 Mb). If the residual gas is mostly bi-atomic molecules, each contributing two electrons, the rate of electron production is [10]

$$\frac{dN_e}{dt} = 2\beta c n_{\text{res}} \sigma_i N(t), \quad (19.52)$$

where  $N(t)$  is the number of protons accumulated from injection at time  $t$ . If  $t_{\text{inj}}$  is the total injection time,  $N(t) = N_p t/t_{\text{inj}}$ , where  $N_p$  is the total number of protons at the end of the injection. The neutralization due to ionization collision at the end of injection is therefore

$$\chi_e = \frac{N_e}{N_p} = \beta c n_{\text{res}} \sigma_i t_{\text{inj}}. \quad (19.53)$$

The vacuum pressure for the ORNL SNS is designed to be  $1 \times 10^{-9}$  Torr and that for the LANL PSR is  $2 \times 10^{-8}$  Torr, while the other ring is with vacuum pressure  $1 \times 10^{-7}$  Torr. The neutralization due to ionization collision turns out to be 0.104%, 1.39%, and 2.33%, respectively, for the ORNL SNS, LANL PSR, and BNL booster. The neutralization factors are large for PSR and the BNL booster because of their relatively low vacuum and long injection times of, respectively,  $\sim 2000$  and 300 turns. The maximum neutralization of the ORNL SNS is small because of the very high vacuum.

Another source of electron production is through the multi-traversing of the stripping foil by the proton beam. For example, a proton in the LANL PSR can generate on the average two electrons because of the presence of the stripping foil.

A more important source of electron production is when an electron hitting the walls of the beam pipe releases secondary electrons. These secondary electrons can cause multi-pactoring and generate a large amount of electrons. Here, we would like to compute the energy of an electron hitting the beam pipe and estimate the efficiency of secondary emission [11].

An electron is oscillating with bounce frequency  $\Omega_e/(2\pi)$  with amplitude increasing exponentially with an e-folding growth rate  $\omega_I$ . Assume that the electron just grazes the wall of the beam pipe at time  $t = 0$ . Its amplitude is given by

$$y = be^{\omega_I t} \cos \Omega_e t, \quad (19.54)$$

where  $b$  is the beam pipe radius. It will hit the other side of the wall at time  $t_1 = (\pi - \Delta)/\Omega_e$ , where

$$-b = be^{\omega_I t_1} \cos \Omega_e t_1 = be^{(\pi - \Delta)\omega_I/\Omega_e} \cos(\pi - \Delta). \quad (19.55)$$

Assuming  $\Delta \ll 1$  and  $\pi\omega_I/\Omega_e \ll 1$ , the solution is

$$\Delta = \sqrt{\frac{2\pi\omega_I}{\Omega_e}} \left[ 1 + \mathcal{O}\left(\sqrt{\frac{\omega_I}{\Omega_e}}\right) \right]. \quad (19.56)$$

The velocity of the electron hitting the other side of the wall can be obtained by differentiating Eq. (19.54) and is given by

$$\dot{y} = -b\sqrt{2\pi\omega_I\Omega_e} \left[ 1 + \mathcal{O}\left(\sqrt{\frac{\omega_I}{\Omega_e}}\right) \right]. \quad (19.57)$$

The kinetic energy is therefore

$$E_{\text{kin}} = \pi m_e \omega_I \Omega_e b^2, \quad (19.58)$$

where  $m_e$  is the electron mass.

For single-electron motion, we can identify the growth rate  $\omega_I = \mu\beta c/\lambda_{rf}$ , where  $\mu$  is given by Eq. (19.4). The velocities and kinetic energies of the electrons hitting the wall on the other side of the beam pipe are listed in Table 19.4. We see that when hitting the beam pipe wall, the electrons possess kinetic energies of 198.6, 775.4, and 139.5 eV, respectively, for the three rings. For the BNL booster, the bunched mode intensity has been used. It is a known fact that an electron in excess of 100 eV hitting a metallic wall will result in a secondary-emission coefficient greater than unity. This implies that multi-pactoring will occur in these three rings. This consideration is for the motion of a single electron and is independent of the amount of electrons present inside the vacuum chamber of the ring. In the design of the ORNL SNS, the beam pipe will be made of stainless steel with a titanium coating, which will reduce the secondary-emission efficiency and thus prevent multi-pactoring to occur. An experiment had been performed at the LANL PSR by coating part of the walls of the vacuum chamber with TiN. The electron flux was found to have been suppressed about 1000 times [15]. However, it was reported at the SLAC PEP low energy positron ring that TiN coating did not help much in reducing electron secondary emission. In passing, it is worth mentioning that aluminum has a much higher second-emission coefficient than stainless steel. Thus, an aluminum vacuum chamber should be avoided if one wish to limit the amount of trapped electrons.

We can also identify  $\omega_I$  with the growth rate  $\tau^{-1}$  of the coherent centroid oscillation in Eq. (19.18). The kinetic energy of an electron hitting the other side of the beam pipe wall becomes

$$E_{\text{kin}} = \frac{\pi m_e Q_p Q_e^{3/2} \omega_0^2 b^2}{2\sqrt{|n - Q_e|}}. \quad (19.59)$$

The kinetic energy of the electron hitting the pipe wall is now proportional to  $Q_p$  and therefore  $\sqrt{\chi_e}$ , the amount of trapped electrons. These results for the three rings are listed in Table 19.4 at the threshold neutralization. Actually, Eq. (19.59) becomes  $E_{\text{kin}} \approx \pi m_e Q_e \omega_0^2 b^2 / 4$  when the threshold values in Eq. (19.22) are substituted. Notice that the kinetic energies of the electrons hitting the beam pipe walls at the onset of coupled-centroid instability are less than 100 eV for the ORNL SNS and the BNL booster in the bunched mode. Thus multi-pactoring will occur only if the neutralization factor is much larger than  $\sim 1\%$ . On the other hand, the electron kinetic energy is 201 eV for the Los Alamos PSR. Thus, multi-pactoring will occur near the onset of coherent centroid instability.

Table 19.4: Kinetic energy of electron hitting the wall of the beam pipe.

	Oak Ridge SNS	Los Alamos PSR	Brookhaven Booster
Total number of protons $N_p$	$2.1 \times 10^{14}$	$4.2 \times 10^{13}$	$2.4 \times 10^{13}$
Beam pipe radius $b$ (m)	0.0500	0.0500	0.0600
<u>Single-electron consideration</u>			
Electron escaping rate $\omega_I$ (MHz)	6.24	13.9	4.69
$\Omega_e$ (MHz)	713.3	1253.9	462.6
Velocity hitting wall $\dot{y}/c$	0.0279	0.0551	0.0234
Kinetic energy hitting wall (eV)	198.6	775.4	139.5
<u>Coherent-centroid-oscillation consideration</u>			
Threshold neutralization $\chi_e$	0.0122	0.0093	0.0132
Growth rate $\omega_I$ (MHz)	1.867	4.392	1.320
$\Omega_e$ (MHz)	572.7	1025.2	325.8
Velocity hitting wall $\dot{y}/c$	0.0137	0.0281	0.0104
Kinetic energy hitting wall (eV)	47.8	201.1	27.6

### 19.2.4 Electron Bounce Frequency

Electron-proton instability is different from other transverse instability in that the bounce frequency of the electrons inside the proton bunch is very broad. Recall that the angular bounce frequency is defined as

$$\Omega_e = \sqrt{\frac{4\lambda r_e c^2}{a_V(a_V + a_H)}}. \quad (19.60)$$

where  $\lambda$  is the linear particle density of the proton bunch. Thus, the bounce frequency of the electrons depends on where they are inside the proton bunch. For example, if the electrons are trapped within the proton FWHM bunch profile, the spread of the bounce frequency will be  $1/\sqrt{2}$  its mean value, which is certainly a wide spread. Another test of the e-p bounce oscillation is to measure the dependency of the bounce frequency on the proton beam intensity. As is given by Eq. (19.60), the bounce frequency should be proportional to the square root of the proton intensity. Such a measurement has been performed at the Los Alamos PSR and is shown in Fig. 19.5. At countdown 1 (CD 1), the longest chopped proton beam is injected from the linac. At  $6.1 \mu\text{C}$  or  $3.81 \times 10^{13}$  proton injected, the electron bounce frequency observed is  $\sim 200$  MHz, very close to

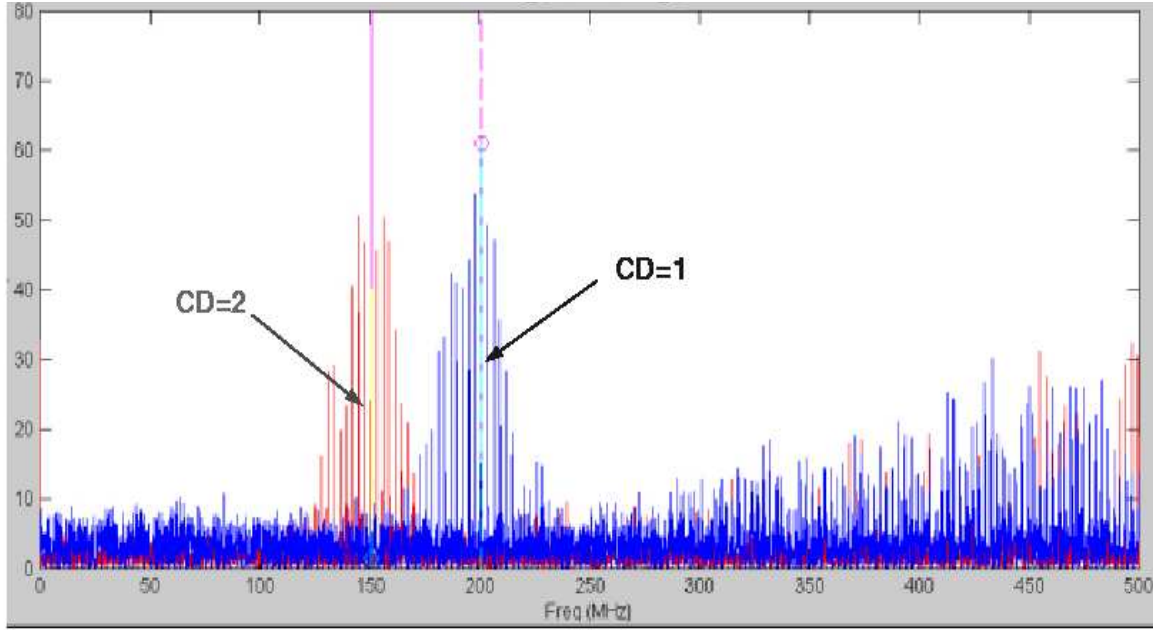


Figure 19.5: (color) The PSR is run at CD 1 with  $6.1 \mu\text{C}$ . The electron bounce frequency is measured to be centered at  $\sim 200$  MHz, close to the theoretical prediction. The total spread of the bounce frequency is roughly 100 MHz, the same order of magnitude as its center value. Operated at CD 2 with  $3.0 \mu\text{C}$ , the bounce frequency reduces to  $\sim 140$  MHz, roughly by  $\sqrt{2}$  times as expected.

the prediction of Eq. (19.60). Next the injection is at countdown 2 (CD 2), where the chopped beam from the linac is injected into the PSR on alternate turns, thus reducing the total injection intensity by half to  $3.0 \mu\text{C}$ . The bounce frequency is found to peak at  $\sim 140$  MHz, very close to a reduction of  $\sqrt{2}$  as predicted. The total spread of the bounce frequency at CD 1 is about 100 MHz, which is also the same order of magnitude as predicted above.

### 19.2.5 Discussion and Conclusion

(1) In the above single-electron analysis, it appears that electrons will be cleared in the bunch gap within one rf wavelength for all the 3 proton rings under consideration. However, if more than  $\eta \sim 4\%$  of the protons are spilled into the bunch gap, electrons will be trapped inside the proton beam in the ORNL SNS and LANL PSR. For the BNL booster, on the other hand, electrons are relatively more difficult to be trapped when

there are spilled protons in the bunch gaps even if  $\eta > 20\%$ . This is probably due to its much larger gap-to-bunch-length ratio.

(2) For coherent centroid oscillation to become unstable, neutralization factors of  $\chi_e \sim 1.2\%$ ,  $0.9\%$ , and  $1.1\%$  are required, respectively, for the three machines. However, spreads in the betatron frequencies and the electron bounce frequencies can provide Landau damping.

(3) The LANL PSR may accumulate protons through an injection in  $\sim 2000$  turns and the BNL booster in 300 turns. The vacuum pressures of both rings are relatively high,  $\sim 1 \times 10^{-8}$  Torr for the former and  $\sim 1 \times 10^{-7}$  Torr for the latter. As a result, the amount of electrons per proton produced by collision with residual gases can be as high as 1.39 and 2.33%, respectively, for the two rings. However, the electron production for the ORNL SNS via proton-ion collision is less than 1%, which is the result of a high vacuum of  $1 \times 10^{-9}$  Torr in the vacuum chamber.

(4) Multi-pactoring as a result of secondary emission will be possible for all the three rings when single electron escapes from the trapping proton beam and hits the metallic beam pipe. For the LANL PSR, multi-pactoring will occur near the onset of coherent centroid instability. However, for the other two rings, multi-pactoring will not occur as soon as centroid oscillations become unstable.

(5) There is a similar proton ring called ISIS at the Rutherford Appleton Laboratory. At the injection energy of 70.4 MeV, about  $2.5 \times 10^{13}$  protons are stored as a continuous coasting beam, which is then captured adiabatically into 2 rf buckets. The protons are ramped to 0.8 GeV when they are extracted. No e-p instabilities have ever been observed at ISIS either running in the bunched mode or the coasting-beam mode. This has always been a puzzle. However, when we compare ISIS with the LANL PSR, we do find some important differences. First, ISIS has a repetition rate of 50 Hz. The injection is fast, about 200 turns. On the other hand, it usually takes about 200 turns for the e-p instability of the PSR to develop to a point when it can be monitored. Second, ISIS has a much larger vacuum chamber, 7 cm in radius. Also the ISIS vacuum chamber is made of ceramic to limit eddy current because of the high repetition rate of 50 Hz. A wire cage is installed inside the ceramic beam pipe to carry the longitudinal return current. The wire cage does not allow transverse image current to flow, thus alleviating in some way the transverse instability. Also the cage wires have much less surface area than the walls of an ordinary metallic beam pipe. As a result, secondary emission will be reduced. The secondary emitted electrons will come out in all directions from the cage

wires. The probability for them to hit another cage wire will be small, thus preventing multi-pactoring to occur. These may be the reasons why e-p instabilities have never been observed at ISIS.

## 19.3 Fast Beam-Ion Instability

In the above sections, we discuss ions trapped in an electron beam (or electrons trapped in a proton beam) causing coherent coupled ion-electron oscillation once the intensity of the trapped ions is high enough. The best cure appears to be a gap between the consecutive bunches. The ions will be cleared in the gap. They will not accumulate inside the potential of the electron beam turn after turn and their intensity will not reach the threshold of coupled-beam instability.

However, if the linear density of the electron beam is large enough and the electron bunch is long enough, even in one pass through a region in the vacuum chamber the electron beam is able to generate and trap so many ions that coupled ion-electron occurs resulting in the emittance growth of the electron beam. This instability, called *fast ion instability*, was first investigated by Raubenheimer and Zimmermann [16]. Instead of a long electron bunch, fast ion instability can also occur for a long train of short electron bunches, because the gaps between consecutive bunches may not be long enough to clear all the ions. This instability is important because of its one pass nature and is not curable by clearing gap. For this reason, this instability can also happen inside a linac.

### 19.3.1 The Linear Theory

In this section, we derive the linear theory of fast ion instability. We will follow the approach of Chao [17]. The only difference is that we need to keep track of the gradual accumulation of ions generated.

Let  $y_e(s|z)$  denotes the vertical displacement of the centroid of a slice of the electron bunch, where  $z$  is the distance of the slice from the head of the electron bunch and  $s$  is the distance along the accelerator. If the head of the bunch passes position  $s = 0$  at time  $t = 0$ ,  $s = vt - z$ , where  $v$  is the beam velocity. We assume that the electron beam contains  $N_e$  electrons, uniformly distribution longitudinally and transversely, has

a length  $\ell$  and horizontal and vertical radii  $a_H$  and  $a_V$ .

Let  $y_I(s, t|z)$  denotes the vertical displacement of the centroid of a slice of the ions at time  $t$  position  $s$  along the accelerator. These ions are generated by the electron slice at a distance  $z$  behind the head of the electron bunch. Since the ions are assumed to have no longitudinal velocity,  $s$  and  $t$  are not related.

### 19.3.1.1 The Ion Equation of motion

Because the focusing force experienced by the ion is relative to the centroid of the electron beam, the equation of motion of the ion is just

$$\frac{\partial^2}{\partial t^2} y_I(s, t|z') + \omega_I^2 [y_I(s, t|z') - y_e(s|vt-s)] = 0 . \quad (19.61)$$

The second argument of the electron displacement has been substituted with  $z = vt - s$  because it is the electron slice at  $z = vt - s$  which are interacting with the ions at location  $s$  and time  $t$ . Here, only the linear force has been included for the linear theory and all image and space charge forces are neglected. The ion bounce angular frequency  $\omega_I$  is given by

$$\omega_I = \sqrt{\frac{4N_e r_p c^2}{\ell a_V (a_V + a_H) A}} , \quad (19.62)$$

where  $r_p$  is the proton classical radius and  $A$  is the atomic mass of the ions. This is exactly the same as the electron bounce frequency we derived in Eq. (19.1) with the electron mass replaced by the ion mass. Although the ion is very much heavier than the electron, the electron beam size is usually very much smaller than the proton beam size. Therefore this ion bounce frequency can be very large also. For a nitrogen ion of  $A = 14$  in an electron bunch containing  $10^{11}$  particles, of total length  $\ell = 1$  cm, and radius  $a = 1$  mm, we find  $\omega_I/(2\pi) = 70$  MHz. In case the beam transverse distribution is bi-Gaussian with rms spreads  $\sigma_H$  and  $\sigma_V$ , the following substituting should be made [16] in Eq. (19.62):

$$a_V (a_V + a_H) \longrightarrow 3\sigma_V (\sigma_V + \sigma_H) . \quad (19.63)$$

The ions described in Eq. (19.61) were produced by proton at location  $s$  (the head is at  $s + z'$ ) at time  $t = (s + z')/v$ , and should have the same distribution as the proton



and has no transverse velocity. Therefore, Eq. (19.61) has the initial conditions

$$\begin{aligned} y_I\left(s, \frac{s+z'}{v} \middle| z'\right) &= y_e(s, z') , \\ \frac{\partial}{\partial t} y_I(s, t | z') \bigg|_{t=\frac{s+z'}{v}} &= 0 . \end{aligned} \quad (19.64)$$

These initial conditions offer a way to determine the ion distribution. A slice of ions, when produced at time  $t_0$ , have exactly same transverse distribution as the slice of electrons. These ions have no initial transverse velocity, but they will start their oscillation about the centroid of the electron slice according to  $r \cos \omega_I(t - t_0)/v$ , with  $r$  being the initial distance of a particular ion from the centroid of the electron slice. This implies that this slice will first contract to zero in one quarter of a betatron oscillation and expand again. Of course, we will not find the ions contract to zero at a location at any time, because at the same location there are other slices of ions produced by other slices of electrons. These ion slice will have different betatron phases than the one that we are talking about, because the electron slice producing them are at different  $z$  from the head of the beam. Because of the betatron oscillation (even in the absence of couple ion-beam oscillation), the average horizontal and vertical radii of the ion slice will be smaller than those of the electron beam. They are just  $a_H/\sqrt{2}$  and  $a_V/\sqrt{2}$  if the distribution of the ions is assumed to be uniform.

A derivation of the ion distribution is as follow. For simplicity, in this derivation a round electron beam with  $a = a_H = a_V$  is assumed. If  $\Sigma$  is the ionization cross section and  $n_g$  is the residual gas density in the vacuum chamber, the linear density of ions

$$\lambda_I = \Sigma n_g N_e \quad (19.65)$$

is produced near the tail of the electron beam, after a total of  $N_e$  electrons have passed through. Now an electron slice of width  $dz'$  at distance  $z'$  behind the head of the electron beam will produce a slice of ions with linear density  $\Sigma n_g N_e dz'/\ell$ . This slice of ions will have radius  $a$  when born. These ions do not move longitudinally. When the electron slice at distance  $z$  behind the head reaches these ions, this ion slice shrinks to the radius  $a \cos \omega_I(z - z')/v$ . Summing up the ions produced by all the electron slices up to the slice at  $z$ , the transverse ion density within a circle of radius  $r$  is

$$\begin{aligned} n_I(r|z) &= \frac{\Sigma n_g N_e}{\pi a^2 \ell} \int_0^z \frac{dz'}{\left( \left| \cos \frac{\omega_I(z-z')}{v} \right| < \frac{r}{a} \right) \cos^2 \frac{\omega_I(z-z')}{v}} \\ &= \frac{\Sigma n_g N_e v}{\pi a^2 \ell \omega_I} \tan \frac{\omega_I z}{v} \bigg|_{0, \left( \left| \cos \frac{\omega_I(z-z')}{v} \right| < \frac{r}{a} \right)} . \end{aligned} \quad (19.66)$$

Now

$$\left| \cos \frac{\omega_I(z')}{v} \right| < \frac{r}{a} \longrightarrow \left| \tan \frac{\omega_I(z')}{v} \right| < \frac{\sqrt{a^2 - r^2}}{r} . \quad (19.67)$$

Thus, in each  $\pi$  period,  $\left| \tan \frac{\omega_I z'}{v} \right|$  receives the contribution of  $\frac{2\sqrt{a^2 - r^2}}{r}$ . When  $\omega_I z/c \gg 1$ , from  $z' = 0$  to  $z$  there are  $\omega_I z/(v\pi)$  such periods. The transverse ion distribution is therefore

$$n_I(r|z) \approx \frac{2\Sigma n_g N_e z}{\pi^2 a^2 \ell} \frac{\sqrt{a^2 - r^2}}{r} . \quad (19.68)$$

This distribution has rms radius  $a/2$ . However, a uniform beam of radius  $a$  has rms radius  $a/\sqrt{2}$ . If we approximate the ion distribution to be uniform, it corresponds to a radius of  $a/\sqrt{2}$ .

### 19.3.1.2 The Electron Equation of Motion

Similar to the ion oscillation in the electron beam, the electron beam also oscillates in the ions. Near the very end of the electron beam, the ions generated by the passage of the whole beam has linear density  $\lambda_I = \Sigma n_g N_e$ . The bounce angular frequency of the last slice of the electron beam in the ions is therefore

$$\omega_e = \sqrt{\frac{8\Sigma n_g N_e r_e c^2}{\gamma a_V (a_V + a_H)}} . \quad (19.69)$$

Comparing with the ion bounce frequency  $\omega_i$  in Eq. (19.62), the  $\gamma$  in the denominator indicates the longitudinal motion of the electron, and the extra factor of 2 in the numerator reminds us that the radii of the ions are smaller than those of the electron beam by  $\sqrt{2}$ . For bi-Gaussian distribution, the substitution  $a_V(a_V + a_H) \rightarrow 6\sigma_V(\sigma_V + \sigma_H)$  should be made. If the residual pressure inside the vacuum chamber is low, this electron bounce frequency is usually small. Take our previous example. If the residual pressure is  $p = 10^{-9}$  Torr, the residual gas density is  $n_g = 3.2 \times 10^{13}$  molecules/m<sup>3</sup> according to Eq. (19.51). For carbon monoxide, the ionization cross section is  $\Sigma = 2.0$  Mb, ion linear density at the tail of the electron bunch is  $\lambda_I = 640$  m<sup>-1</sup>, and the electron bounce frequency is  $\omega_e/(2\pi) = 1.3$  kHz. For an electron slice at distance  $z < \ell$  behind the head of the electron beam, the bounce frequency becomes  $\omega_e \sqrt{z/\ell}$  because only  $N_e z/\ell$  electrons have participated in the ion production. The equation of motion for the centroid of a slice of the electron beam can therefore be written as

$$v^2 \frac{\partial^2}{\partial s^2} y_e(s|z) + \omega_\beta^2 y_e(s|z) + \frac{\omega_e^2 z}{\ell} \left[ y_e(s|z) - \frac{1}{z} \int_0^z dz' y_I\left(s, \frac{s+z'}{v} \middle| z'\right) \right] = 0 , \quad (19.70)$$

where  $\omega_\beta$  is the angular betatron frequency due to external focusing. The last term in the square brackets denotes the centroid of the ion slice produced by those electrons electron beam from the head to the length  $\ell$  of the electron beam, where a uniform longitudinal distribution of the electron beam has been assumed.

### 19.3.1.3 Coupled-Ion-Beam Solution

The coupled ion-beam motion, Eqs. (19.61) and (19.70), is solved by separating the fast oscillating part and slow amplitude evolution part. We would like to obtain the asymptotic behavior of the beam-ion system. Let us make our observation at a fixed location  $s$  when there is a resonance between the beam and ions. the electron slice  $z$  behind the head of the electron bunch passes this location, it should have the same fast oscillating frequency as the ions at the same location. The fast oscillating part of the electron slice is

$$y_e(s|z) \sim e^{-i\omega_\beta s/v + ikz} \sim e^{-i\omega_\beta s/v + ikvt - iks}, \quad (19.71)$$

where  $k$  is to be determined and  $z = vt - s$  has been substituted. The ions execute simple harmonic motion like

$$y_I(s, t|z') \sim y_I(s, t_0|z') e^{\pm i\omega_I(t-t_0)}. \quad (19.72)$$

At the time  $t_0 = (s + z')/v$  when the ions are born (for any  $z' < \ell$ ), since they should have the same displacement as the electrons that produce them, therefore

$$\begin{aligned} y_I(s, t|z') &\sim y_e(s|z') e^{\pm i\omega_I(t-t_0)} \\ &\sim e^{-i\omega_\beta s/v + ikz'} e^{\pm i\omega_I t \mp i\omega_I(s+z')/v}. \end{aligned} \quad (19.73)$$

Comparing the time dependency of Eqs (19.71) and (19.73), for a resonance to occur we must have

$$k = \omega_I v. \quad (19.74)$$

The other solution,  $k = -\omega_I v$ , will lead to a decaying oscillatory solution which is of no interest to us (see below).

After determining the fast oscillating part at a resonance, now let

$$\begin{aligned} y_e(s|z) &\sim \tilde{y}_e(s|z) e^{-i\omega_\beta s/v + i\omega_I z/v}, \\ y_I(s, t|z') &\sim \tilde{y}_I(s, t|z') e^{-i(\omega_\beta + \omega_I)s/v + i\omega_I t}, \end{aligned} \quad (19.75)$$

where  $\tilde{y}_e(s|z)$  and  $\tilde{y}_I(s, t|z')$  are slowly varying in  $s$  and  $t$ , respectively. Substitute Eq. (19.75) into Eqs. (19.61) and (19.70), and neglecting second order derivatives of  $\tilde{y}_e(s|z)$  and  $\tilde{y}_I(s, t|z')$ , we obtain

$$\frac{\partial}{\partial t} \tilde{y}_I(s, t|z') + \frac{i\omega_I}{2} \tilde{y}_e(s|vt-s) = 0 , \quad (19.76)$$

$$\frac{\partial}{\partial s} \tilde{y}_e(s|z) + \frac{i\omega_e^2}{2\omega_\beta v \ell} \left[ z \tilde{y}_e(s|z) - \int_0^z dz' \tilde{y}_I\left(s, \frac{s+z}{v} \middle| z'\right) \right] = 0 , \quad (19.77)$$

with the initial condition

$$\tilde{y}_I\left(s, \frac{s+z'}{v} \middle| z'\right) = \tilde{y}_e(s|z') . \quad (19.78)$$

The first equation can be integrated to give

$$\begin{aligned} \tilde{y}_I(s, t|z') &= \tilde{y}_I\left(s, \frac{s+z'}{v} \middle| z'\right) - \frac{i\omega_e}{2} \int_{\frac{s+z}{v}}^t dt' y_e(s|vt'-s) \\ &= \tilde{y}_e(s|z') - \frac{i\omega_e}{2v} \int_{z'}^{vt-s} dz'' y_e(s|z'') . \end{aligned} \quad (19.79)$$

Substituting into the second equation, we get

$$\frac{\partial}{\partial s} \tilde{y}_e(s|z) + \frac{i\omega_e^2}{2\omega_\beta v \ell} \left[ z \tilde{y}_e(s|z) - \int_0^z dz' y_e(s|z') \right] + \frac{i\omega_e^2}{2\omega_\beta v \ell} \frac{i\omega_I}{2v} \int_0^z dz' \int_{z'}^z dz'' \tilde{y}_e(s|z'') = 0 . \quad (19.80)$$

Integrating by part, it is easy to show that

$$\begin{aligned} z \tilde{y}_e(s|z) - \int_0^z dz' \tilde{y}_e(s|z') &= \int_0^z dz' z' \frac{\partial}{\partial z'} \tilde{y}_e(s|z') , \\ \int_0^z dz' \int_{z'}^z dz'' \tilde{y}_e(s|z'') &= \int_0^z dz' z' \tilde{y}_e(s|z') . \end{aligned}$$

Then we arrive at

$$\frac{\partial}{\partial s} \tilde{y}_e(s|z) + \frac{i\omega_e^2}{2\omega_\beta v \ell} \left[ \int_0^z dz' z' \frac{\partial}{\partial z'} \tilde{y}_e(s|z') + \frac{i\omega_I}{2v} \int_0^z dz' z' \tilde{y}_e(s|z') \right] . \quad (19.81)$$

Another differentiating with transform the differential-integral equation into a differential equation:

$$\frac{\partial^2}{\partial s \partial z} \tilde{y}_e(s|z) + \frac{i\omega_e^2}{2\omega_\beta v \ell} z \left[ \frac{\partial}{\partial z} \tilde{y}_e(s|z) + \frac{i\omega_I}{2v} \tilde{y}_e(s|z) \right] . \quad (19.82)$$

Earlier, we have estimated that the ion bounce frequency is usually very high. If the growth rate of the electron beam envelope is small, we can neglect the first term in the square brackets. Then, Eq. (19.82) will be very much simplified to

$$\frac{\partial^2}{\partial s \partial z} \tilde{y}_e(s|z) + \frac{i\omega_e^2 \omega_I}{4\omega_\beta v^2 \ell} z \tilde{y}_e(s|z) = 0 . \quad (19.83)$$

The solution is that  $\tilde{y}_e(s|z)$  depends on  $s$  and  $z$  through one dimensionless variable

$$\eta = \frac{z}{\ell} \sqrt{\frac{\omega_e^2 \omega_I \ell s}{2\omega_\beta v^2}} , \quad (19.84)$$

and Eq. (19.83) becomes

$$\eta \frac{d^2 \tilde{y}_e}{d\eta^2} + \frac{d\tilde{y}_e}{d\eta} - \eta \tilde{y}_e = 0 . \quad (19.85)$$

which is just the modified Bessel equation. Thus, we obtain the simple solution

$$\tilde{y}_e(s, z) = y_0 I_0(\eta) , \quad (19.86)$$

where  $I_0$  is the modified Bessel function of order zero, while  $y_0 = \tilde{y}_e(s|0)$  is the amplitude of oscillation of the head of the bunch if we make observation at a fixed location  $s$ , or  $y_0 = \tilde{y}_e(0|z)$  is the initial amplitude of the centroid of a slice in the electron beam. In the asymptotic regime with  $\eta \gg 1$ , we have

$$\tilde{y}_e(s, z) = y_0 \frac{e^\eta}{\sqrt{2\pi\eta}} . \quad (19.87)$$

Thus the asymptotic growth of the oscillating amplitude is exponential in  $z$  along the electron beam. However, for a fixed slice (fixed  $z$ ), the growth of the amplitude is exponential in  $\sqrt{s}$ . If we have chosen  $k = -\omega_I v$  as the resonance condition in Eq. (19.74), the solution of Eq. (19.87) would have become

$$\tilde{y}_e(s, z) \sim \frac{e^{\pm i|\eta|}}{\sqrt{2\pi|\eta|}} , \quad (19.88)$$

which is oscillatory and slowing decreasing. In fact, Eq. (19.85) becomes the Bessel equation and the solution becomes  $J_0(|\eta|)$ .

Observing at a fixed location  $s$ , we can define a growth length (in time) along the bunch

$$\tau_0 = \sqrt{\frac{2\omega_\beta \ell}{\omega_e^2 \omega_I s}} . \quad (19.89)$$

One may expect this growth time not dependent on the total length of the bunch. In fact, this is true, because from Eq. (19.69)  $\omega_e^2/\tau_L$  depends only on the linear density of the electron beam. If we are monitoring a specific slice of the electron beam (at fixed  $z$  or  $\tau = z/v$  in time behind the head) as a function of time  $t$  or  $s = vt$  along the accelerator, we can define a growth time for a roughly  $e$ -folding,

$$t_0 = \frac{2\omega_\beta\tau_L}{\omega_e^2\omega_I\tau^2} , \quad (19.90)$$

which is also independent of the electron bunch length  $\tau_L = \ell/v$ .

Knowing the asymptotic behavior of the amplitude of the electron bunch, we can compute the same for the ions. Substituting Eq. (19.87) into the second term on the right side of Eq. (19.79), we obtain

$$\tilde{y}_I(s, t|z') \approx -iy_0 \sqrt{\frac{\omega_\beta\omega_I\ell}{2\omega_e^2s}} \frac{e^\eta}{\sqrt{2\pi\eta}} \Big|_{z=vt-s} . \quad (19.91)$$

This tells us that the first term on the right side of Eq. (19.79) can be neglected because it is  $\sqrt{\omega_\beta\omega_I\ell/(2\omega_e^2s)}$  smaller. Therefore when the ions meet the electron slice  $z$  behind the head of the electron bunch at location  $s$ , the ratio of the ion displacement to the beam displacement is

$$\frac{y_I(s, t|z')}{y_e(s|z)} \Big|_{z=vt-s} = \frac{\tilde{y}_I(s, t|z')}{\tilde{y}_e(s|z)} \Big|_{z=vt-s} \approx -i \sqrt{\frac{\omega_\beta\omega_I\ell}{2\omega_e^2s}} . \quad (19.92)$$

Thus the ion oscillation is  $90^\circ$  out of phase relative to the electrons, and the ion amplitude is very much larger according to the example we demonstrated earlier.

We can now check the validity of a previous approximation of neglecting the first term in the square brackets of Eq. (19.82), which implies the necessity of

$$\left| \frac{\partial}{\partial z} \tilde{y}_e(s|z) \right| \ll \left| \frac{\omega_I}{2v} \tilde{y}_e(s|z) \right| . \quad (19.93)$$

Knowing the asymptotic behavior of the electron beam, this is equivalent to requiring

$$\frac{\eta}{z} = \sqrt{\frac{\omega_e^2\omega_I s}{2\omega_\beta\ell}} \ll \frac{\omega_I}{2} . \quad (19.94)$$

Using the definition of the growth time  $\tau_0$  [Eq. (19.89)] along the electron beam, this requirement is just

$$\frac{\omega_I \tau_0}{2} \gg 1. \quad (19.95)$$

In other words, the beam makes many oscillations within one growth length along the beam.

### 19.3.2 Spectrum of Electron Beam

Observing at location  $s = 0$ , the spectrum  $\tilde{\rho}\Omega$  of the electron beam is given by

$$\tilde{\rho}(\Omega) \propto \int_0^\infty dt e^{-i\Omega t} \sum_{k=0}^\infty y_e(kC|vt - kC) \Big|_{0 < vt - kC < \ell}, \quad (19.96)$$

where  $C = 2\pi R = vT_0$  is the ring circumference and  $k$  sums over multiple turns. We next transform the integration to  $t$  within one turn only. Thus

$$\begin{aligned} \tilde{\rho}(\Omega) &\propto \sum_{k=0}^\infty \int_0^{\ell/v} dt e^{-i\Omega(t+kT_0)} y_e(kC|vt) \\ &= \sum_{k=0}^\infty e^{-i(\Omega+\omega_\beta)kT_0} \int_0^{\ell/v} dt e^{-i(\Omega-\omega_I)t} \tilde{y}_e(kC|vt) \\ &= \sum_{k=0}^\infty e^{-i(\Omega+\omega_\beta)kT_0} \int_0^{\ell/v} dt e^{-i(\Omega-\omega_I)t} \frac{y_0 e^{\eta'}}{\sqrt{2\pi\eta'}}, \end{aligned} \quad (19.97)$$

with

$$\eta' = t \sqrt{\frac{\omega_e^2 \omega_I kC}{2\omega_\beta \ell}}. \quad (19.98)$$

The integral, denoted by  $I$ , can be performed exactly in terms of the incomplete gamma function  $\gamma$ . We obtain

$$I = \int_0^{\ell/v} dt \frac{e^{(B-ia)t}}{\sqrt{2\pi Bt}} = \frac{1}{\sqrt{2\pi B}} (-B + iA)^{-1/2} \gamma \left[ \frac{1}{2}, \frac{(-B + iA)\ell}{v} \right], \quad (19.99)$$

where  $A = \Omega - \omega_I$  and  $B = \eta'/t'$ . When  $|x| \gg 1$ , we have  $\gamma(\alpha, x) \approx -x^{\alpha-1} e^{-x}$ , and

$$I \approx e^{B\ell/v} \sqrt{\frac{\ell}{2\pi Bv}} \left( \frac{e^{-iA\ell/(2v)} \sin \frac{A\ell}{2v}}{\frac{A\ell}{v}} \right), \quad (19.100)$$

where  $|A|\ell/v \gg B\ell/v \gg 1$  has been used. The summation over  $k$  diverges because the signal itself diverges. However, if we measure in a small window around some large  $k = \bar{k}$ , we obtain the spectrum

$$|\tilde{\rho}(\Omega)| \propto y_0 e^{\bar{B}\ell/v} \sqrt{\frac{\ell}{2\pi\bar{B}v}} \left| \frac{\sin \frac{(\Omega - \omega_I)\ell}{2v}}{\frac{(\Omega - \omega_I)\ell}{2v}} \right| \sum_{p=-\infty}^{\infty} \delta(\Omega - p\omega_0 + \omega_\beta) , \quad (19.101)$$

where  $\omega_0$  is the revolution angular frequency and  $\bar{B}$  is the former  $B$  when  $k$  replaced by  $\bar{k}$ . The spectrum observed is therefore all the lower betatron sidebands modulated by the sinc function which peaks at  $\omega_I$  with a width equals to the inverse length of the electron beam.

### 19.3.3 Possible Cures

There are several methods to overcome this fast beam-ion instability. Simulations shows that the oscillation amplitude of the trailing beam particles saturates at about one  $\sigma_v$  due to nonlinear character of the coupling force. Thus, if we can reduce the original vertical emittance by a factor of two, the saturated emittance will be approximately what is desired. Another method is to have a lattice of the accelerator ring in which the product of the horizontal and vertical betatron functions changes substantially as a function of position along the ring. The transverse beam size of the beam will have such large variation accordingly. As a result, the ion bounce frequency  $\omega_I$  will vary significantly with time and no coherent oscillation can therefore develop. A third remedy is to introduce gaps within the beam if it is very long. In case of a bunch train, the introduction of additional longer bunch gaps will certainly help. As an example, additional 10 bunch gaps in PEP-II increase the instability rise time from 0.5  $\mu s$  to 0.5 ms, which is inside the bandwidth of the feedback system. For linacs, the trailing bunches of a long train may be realigned by use of fast kickers and feedback.

### 19.3.4 Applications

Raubenheimer and Zimmermann applied the linear theory of fast beam-ion instability to some existing accelerators like the SLAC Linear Collider (SLC) arc, the SLC positron Damping Rings (DR), the LBL Advanced Light Source (ALS), the DESY HERA, the



Table 19.5: Parameters and oscillation growth rates for some existing accelerators.

Accelerator	SLC arc	SLC e <sup>+</sup> DR	ALS	HERA e <sup>-</sup>	CESR	ESRF
$\epsilon_x^N$ (m)	$5 \times 10^{-5}$	$3 \times 10^{-5}$	$1.2 \times 10^{-5}$	$2 \times 10^{-3}$	$2.7 \times 10^{-3}$	$7.5 \times 10^{-5}$
$\epsilon_y^N$ (m)	$5 \times 10^{-6}$	$3 \times 10^{-6}$	$2 \times 10^{-7}$	$1.1 \times 10^{-4}$	$1.2 \times 10^{-4}$	$7.5 \times 10^{-6}$
$n_b$	1	1	328	210	7	330
$N_b$	$3.5 \times 10^{10}$	$4 \times 10^{10}$	$7 \times 10^9$	$3.7 \times 10^{10}$	$4.6 \times 10^{11}$	$5 \times 10^9$
$\beta_{x,y}$	4	1, 3	2.5, 4	25	14, 13	8, 8
$\bar{\beta}_y$	4	3	4	25	13	8
$\sigma_x$ ( $\mu$ m)	47	113	101	991	1965	226
$\sigma_y$ ( $\mu$ m)	15	62	17	232	399	71
$\ell$ or $\sigma_z$	1 mm	5.9 mm	200 m	6048 m	670 m	280 m
$E$ (GeV)	46	1.2	1.5	26	5	6
$p$ (Torr)	$10^{-5}$	$10^{-8}$	$10^{-9}$	$10^{-9}$	$5 \times 10^{-9}$	$2 \times 10^{-9}$
particle	e <sup>+</sup>	e <sup>+</sup>	e <sup>-</sup>	e <sup>-</sup>	e <sup>-</sup>	e <sup>-</sup>
$\omega_I/(2\pi)$ (MHz)	$3.6 \times 10^5$	$4.6 \times 10^4$	31	0.87	0.92	6.8
$\omega_\beta/(2\pi)$ (MHz)	11.9	15.9	11.9	1.91	3.67	5.96
$\omega_e/(2\pi)$ (MHz)	0.481	0.029	0.149	0.0054	0.0098	0.027
Single or multibunch	single	single	multi	multi	multi	multi
$t_0$ ( $z \approx \ell$ )	1.09 $\mu$ s	511 $\mu$ s	1.30 $\mu$ s	187 $\mu$ s	942 $\mu$ s	65 $\mu$ s

Cornell Electron Storage Ring (CESR), and the European Synchrotron Radiation Facility (ESRF). The results<sup>†</sup> are shown in Table 19.5. Applications are also made to some future accelerators, like the Next Linear Collider (NLC) electron and positron Damping Rings (DR), the NLC Main Linac, the NLC Pre-Linac, the PEP-II Higher Energy Ring<sup>‡</sup> (HER), the KEK Accelerator Test Facility (ATF) Damping Ring. The results are shown in Table 19.6. In the tables, some are data for the accelerators and some are computed numbers. For example, the beam transverse rms sizes,  $\sigma_{x,y}$ , are computed from the given normalized rms emittances  $\epsilon_{x,y}^N$  and betatron functions  $\beta_{x,y}$ . In computing the ion bounce frequency  $\omega_I/(2\pi)$ , the beam linear density is taken at the peak density in case the beam considered is a single bunch, and as an average in case the beam considered is a train of bunches. In computing the beam particle bounce frequency  $\omega_e/(2\pi)$ , an ionization cross section of 2 Mb has been assumed. In computing the growth time  $t_0$ ,

<sup>†</sup>In some cases, our computed numbers are different from what are given in Ref. [16].

<sup>‡</sup>This ring is in operation now. But it was under construction at the time Ref. [16] was written.

Table 19.6: Parameters and oscillation growth rates for some future accelerators.

Accelerator	NLC e <sup>-</sup> DR	NLC e <sup>+</sup> DR	NLC Pre-linac	NLC Main linac	PEP-II HER	ATF DR
$\epsilon_x^N$ (m)	$3 \times 10^{-6}$	$3 \times 10^{-6}$	$3 \times 10^{-6}$	$3 \times 10^{-6}$	$5 \times 10^{-4}$	$3 \times 10^{-6}$
$\epsilon_y^N$ (m)	$3 \times 10^{-8}$	$3 \times 10^{-8}$	$3 \times 10^{-8}$	$3 \times 10^{-8}$	$2.5 \times 10^{-5}$	$3 \times 10^{-8}$
$n_b$	90	90	90	90	1658	60
$N_b$	$1.5 \times 10^{10}$	$1.5 \times 10^{10}$	$1.5 \times 10^{10}$	$1.5 \times 10^{10}$	$3 \times 10^{10}$	$1 \times 10^{10}$
$\beta_{x,y}$	0.5, 5	0.5, 5	6	8	15	0.5, 5
$\bar{\beta}_y$	2	2	6	8	15	2.5
$\sigma_x$ ( $\mu$ m)	62	62	68	35	1060	22
$\sigma_y$ ( $\mu$ m)	3.9	3.9	6.8	3.5	169	7.1
$\ell$ or $\sigma_z$	38 m	4 mm	38 m	38 m	2000 m	50 m
$E$ (GeV)	2	2	2	10	9	1.54
$p$ (Torr)	$10^{-9}$	$10^{-9}$	$10^{-8}$	$10^{-8}$	$10^{-9}$	$6 \times 10^{-8}$
particle	e <sup>-</sup>	e <sup>+</sup>	e <sup>-</sup>	e <sup>-</sup>	e <sup>-</sup>	e <sup>-</sup>
$\omega_I/(2\pi)$ (MHz)	151	$2.23 \times 10^5$	108	209	4.46	98.2
$\omega_\beta/(2\pi)$ (MHz)	23.9	23.9	7.95	5.96	3.18	19.1
$\omega_e/(2\pi)$ (MHz)	0.271	0.029	0.613	0.531	0.027	1.78
Single or multibunch	multi	single	multi	multi	multi	multi
$t_0$ ( $z \approx \ell$ )	856 ns	124 $\mu$ s	78 ns	40 ns	7.2 $\mu$ s	19 ns

the bunch length is taken as  $\ell = 2\sigma_z$  in case the beam considered is a single bunch. With the exception of HERA and PEP-II HER, we find

$$\omega_e \ll \omega_\beta \ll \omega_I . \quad (19.102)$$

But in all cases, we do have

$$\omega_e \ll \omega_I . \quad (19.103)$$

For the existing accelerators, all the rise times are longer than the synchrotron damping times, except for the ALS and ESRF. Transverse instabilities have been reported in the ALS; but they are not necessary caused by ions. For the ESRF, the expected fast beam-ion instability growth time is about a factor 150 smaller than the radiation damping time. But so far there is no evidence for ion-related effects or multibunch instability at the ESRF. One possible explanation for the observed stability pertains to the distinct focusing optics: a Chasman-Green lattice, in which the product of the horizontal and

vertical betatron functions varies by more than a factor of 100 around the ring. This will lead to a variation of the ion bounce frequency by an order of magnitude. The decoherence of the ion motion due to this large frequency variation could effectively suppress the instability. On the other hand, this source of decoherence does not exist in a FODO lattice where the product of the transverse beam sizes is nearly constant. It is fortunate that the fast beam-ion instability was discovered when the B-factories at SLAC and KEK were still under construction. Theoretical and experimental analyses had been performed to make sure that this instability would be avoided.

#### 19.3.4.1 Observation at ALS

The fast beam-ion instability had been demonstrated experimentally at the LBL ALS, the Pohang Light Source (PLS), and the KEK TRISTAN [18, 19, 20]. The ALS has 328 rf buckets. In the experiment, only up to 240 consecutive buckets were filled so that there was a large gap to make sure that ions would not be trapped turn after turn. Unlike the experiment at the PLS, the feedback damping was turned on to suppress any coupled-bunch instabilities. Thus if any beam-ion instabilities developed, they would be due to single-pass generated ions. The pressure in the vacuum chamber was elevated to  $\sim 80 \times 10^{-9}$  Torr by injected He. The onset of instability was carefully monitored by increasing the length of the bunch train slowly. Starting with a single bunch at 0.5 mA, consecutive bunches were filled slowly and the vertical beam size was measured. Figure 19.6 plots the rms beam size as a function of number of bunches in the train. We see that at elevated pressure with He added, the beam size increases strongly with number of bunches and becomes saturated when number of bunches exceed 8. We also see that at normal operating vacuum pressure, the beam size does not vary with the number of bunches in the train. The spectrum of the bunch train was also measured when the train contained 240 bunches, but with the total bunch intensity varied. The results in the left plots of Fig. 19.7 show the vertical betatron sidebands (the difference of the upper-sideband amplitude and the lower-sideband amplitude) clustered about 10 MHz when the total bunch current is 82 mA. As the current was raised to 142 mA and 212 mA, we see that the cluster of sidebands move to higher frequencies. If this is the fast beam-ion instability, these sideband frequencies are just the ion bounce frequencies. Figure 19.7 plots the measured ion bounce frequency as a function of beam current along with the theoretical prediction given by Eq. (19.62). We see that the theory fits the experimental data rather well.

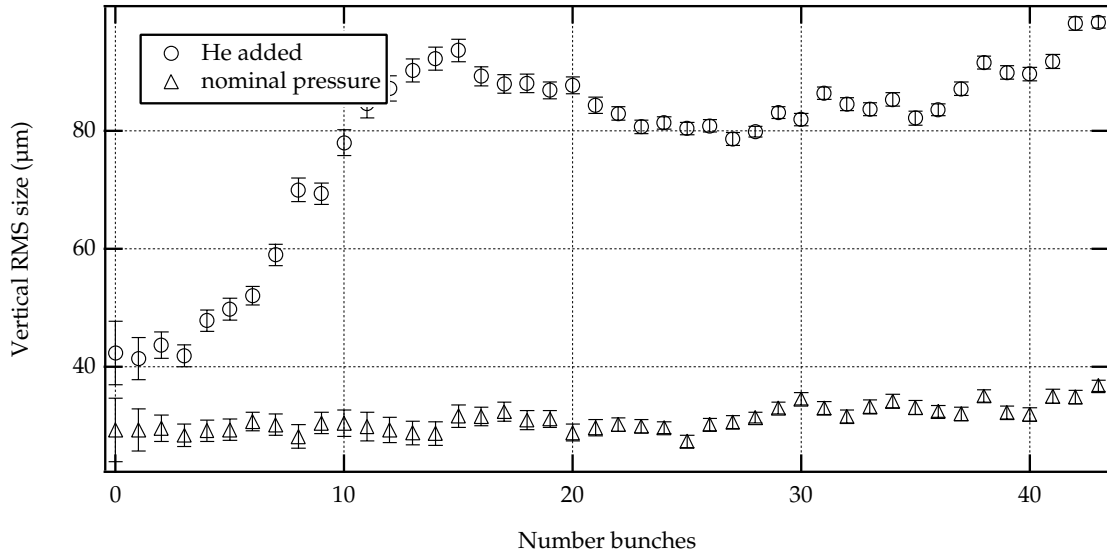


Figure 19.6: Rms vertical beam size versus the number of bunches for nominal and elevated pressure conditions.

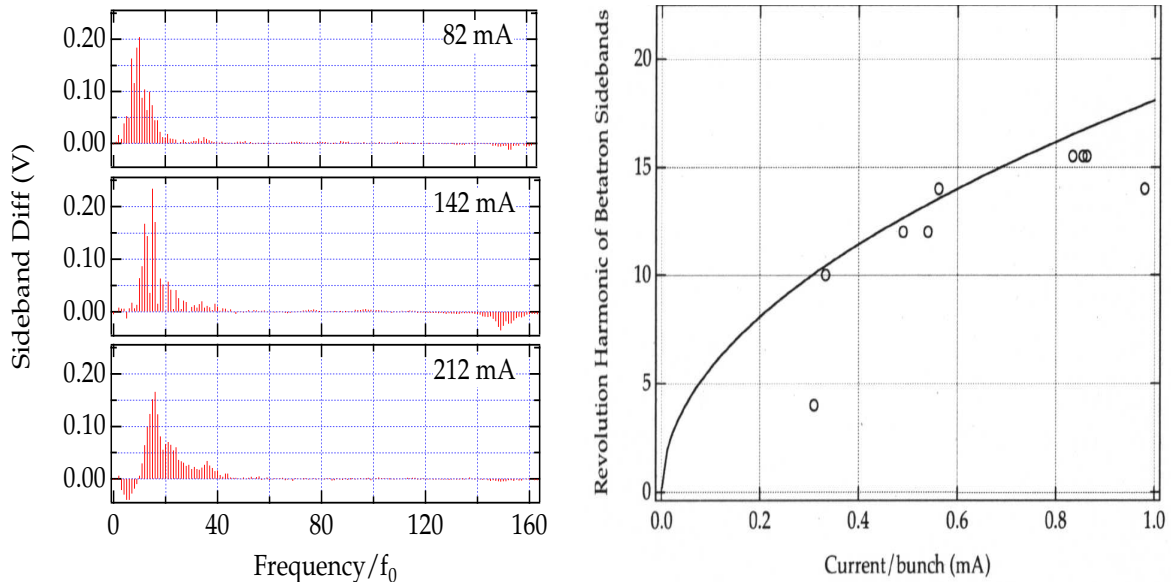


Figure 19.7: (color) Left: Vertical betatron sidebands measured in the 240/328 fill pattern for three different total currents of the bunch train. Right: Comparison between the measured and predicted frequency of coherent beam oscillations as a function of current per bunch for the 240/328 fill pattern.

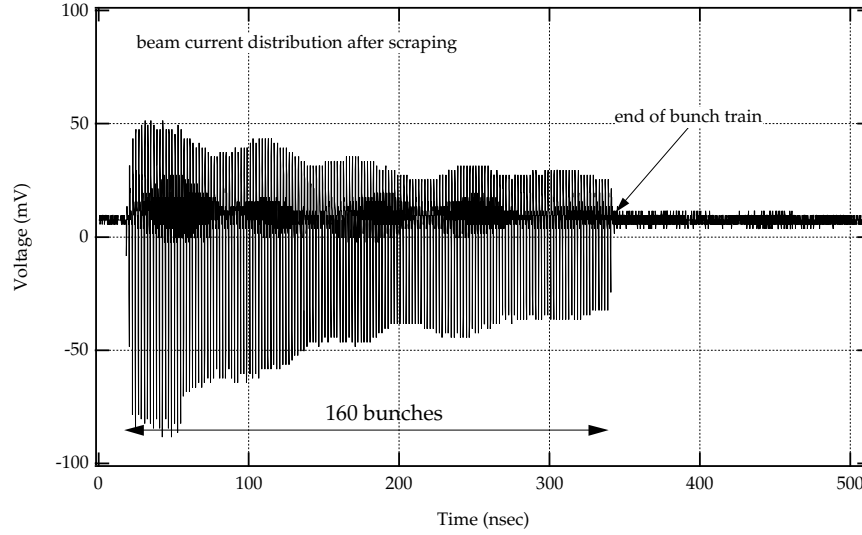


Figure 19.8: Beam current along the bunch train for 160 bunches after scraping a vertical aperture close to the beam. The decreasing bunch current shows the increasing vertical oscillation amplitude along the bunch train (before scraping).

The relative amplitude of oscillations along the bunch train was also measured indirectly. A collimator was used to scrape a train consisting of 160 bunches. After scraping, the bunch intensity was found to be decreasing from the head of the train to the tail. In fact, the scraper reduced the bunch population in the tail about 2.5 times more than that of the leading bunches. This indicates that, before the scraping, the bunch vertical oscillating amplitudes increase along the bunch train.

The growth rate was also estimated and it agreed with the prediction of the linear theory. Thus, All evidence accumulated is qualitatively in consistent with the assumption that the observed instability is the fast beam-ion instability

#### 19.3.4.2 Observation at the Fermilab Linac

Fast transverse oscillations with large amplitudes were observed [21] in the  $H^-$  beam in the 750 keV transfer line of the Fermilab linac in 1988 when the vacuum pressure was raised to  $7 \times 10^{-6}$  Torr to reduce the effect of space charge on the beam [22, 23] and thereby reduce the effective emittance entering the linac. In order not to degrade the performance of the 8 GeV booster, into which the linac injects, this transverse instability

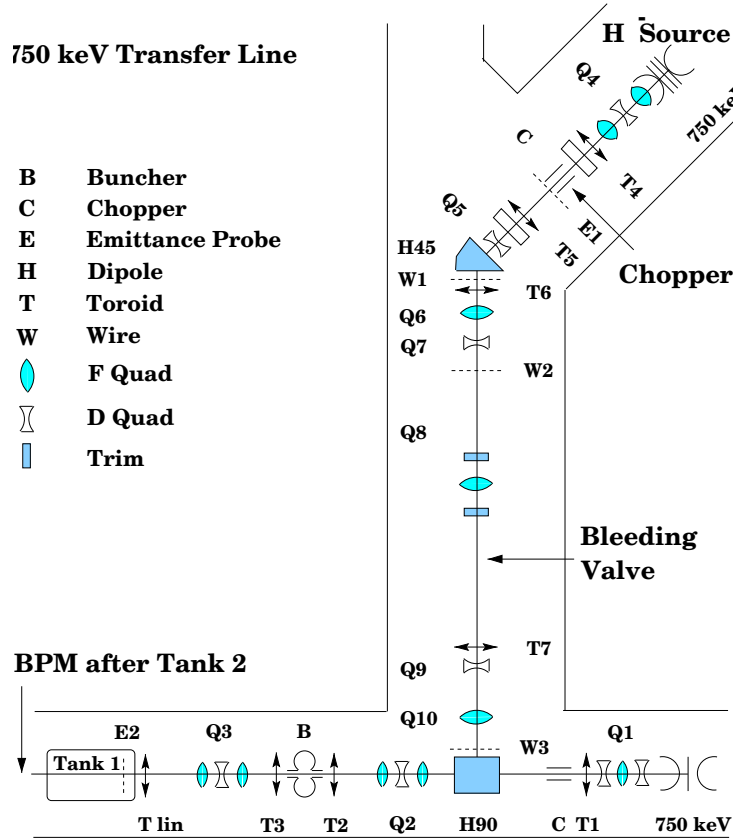


Figure 19.9: The 750 keV transfer line of the Fermilab linac. The length is  $\sim 10$  m from the chopper C to the entry into the linac. Beam current measurements are made by a toroid monitor between Tank 1 and Tank 2, and again further downstream.

has been avoided by choosing the operating vacuum pressure to be  $2.65 \times 10^{-6}$  Torr. The observation resembles the fast beam-ion instability, where individual ions last only for a single passage of the particle beam and need not be trapped. An experiment was performed at the 750 keV transfer line in 2000 in order to further understand the instability previously observed [24].

Figure 19.9 shows the 750 keV transfer line into the main linac. Different gases like hydrogen, helium, nitrogen, argon, and krypton, were injected through the bleeding valve. The gas pressure was controlled by adjusting the rate of flow of gas at the bleeding valve while vigorously pumping at the large ion pumps near the chopper C and the entrance into Tank 1 as well as a small ion pump near the bleeding valve. The

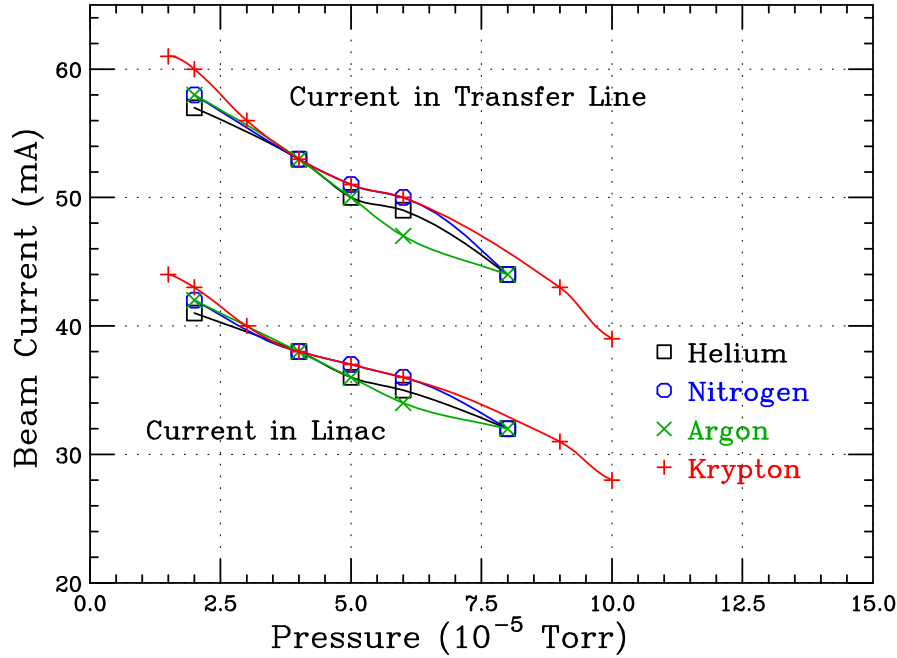


Figure 19.10: (color) Beam current in the transfer line (top) measured by toroids between Tank 1 and Tank 2, and further downstream in the linac (bottom). The drop in beam current at higher vacuum pressure is probably due to the stripping of the electron on the  $H^-$  by the gases injected.

pressure monitored near the three ion pumps showed steady readings. In this way the vacuum pressure could be varied between  $1 \times 10^{-5}$  and  $1 \times 10^{-4}$  Torr, while the normal operating vacuum pressure has been  $2.65 \times 10^{-6}$  Torr. A toroidal monitor near the exit of Tank 1 and entrance of Tank 2 measured the beam current. We see in Fig. 19.10 that the beam current in the transfer line (top) decreases with pressure. This is mostly due to the stripping of the electron on  $H^-$  by collision with the gas particles so that the resulting neutral H particles could not follow the dipole bend H90 into the current monitor. Another current monitor downstream measured the beam current in the linac downstream (bottom). The smaller values observed represent beam loss.

A 750 keV  $H^-$  beam chopped to the length of  $\tau_b = 35 \mu s$  entered the transfer line. Its center position was picked up by the beam-position monitor (BPM) after Tank 2. The signals were recorded using a LeCroy scope and the spectral content was obtained numerically using FFT. To lower the noise level, measurements were averaged over approximately 20 beam pulses. To avoid any signal not related with the beam oscillation, only the last 20  $\mu s$  of the beam pulse were Fourier analyzed. There was no

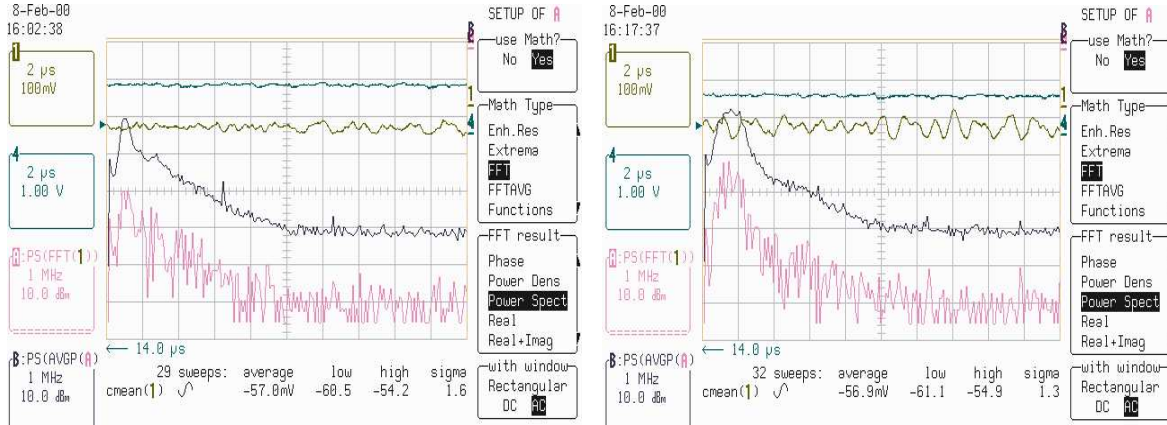


Figure 19.11: (color) Beam intensity (1st trace) and beam horizontal displacement (2nd trace) from the 14th  $\mu\text{s}$  at  $2 \mu\text{s}$  per division, when the injected gas is nitrogen at  $3 \times 10^{-5}$  Torr (left) and  $8 \times 10^{-5}$  Torr (right). The 4th trace is the FFT at 1 MHz per division of the last  $20 \mu\text{s}$  of the beam horizontal displacement. The third trace is the FFT averaged over 20 beam pulses. As pressure increases, the resonant peak becomes broadened and moves towards higher frequencies.

noticeable difference between displacement signals in the horizontal and vertical planes, so all data were taken in the horizontal plane only.

A typical set of results for nitrogen at  $3 \times 10^{-5}$  Torr is shown in the left plot of Fig. 19.11, where the first two traces correspond to the beam intensity and the horizontal beam position, respectively. The 4th trace is the FFT of the beam position for the last  $20 \mu\text{s}$  of the beam, while the 3rd trace depicts the average of 23 FFT beam pulses. We can clearly see a resonant frequency of  $\sim 0.5$  MHz. As the gas pressure was increased to  $8 \times 10^{-5}$  Torr in the right plot of Fig. 19.11, the resonant signal is broadened and spreads out to higher frequencies. Figure 19.12 shows the BPM signals for the horizontal oscillations of the  $\text{H}^-$  beam when argon is introduced. We see rapid growth in oscillation amplitude along the beam. The growth becomes much faster as the gas pressure is increased from  $3 \times 10^{-5}$  to  $1 \times 10^{-4}$  Torr. We also notice that saturation is reached very soon and the growth stops.

### 19.3.4.3 Ionization Cross section

When the velocity of the incident particle is much larger than the velocity of the electron inside the target atom about to be ionized, the impulse approximation can be used. Our



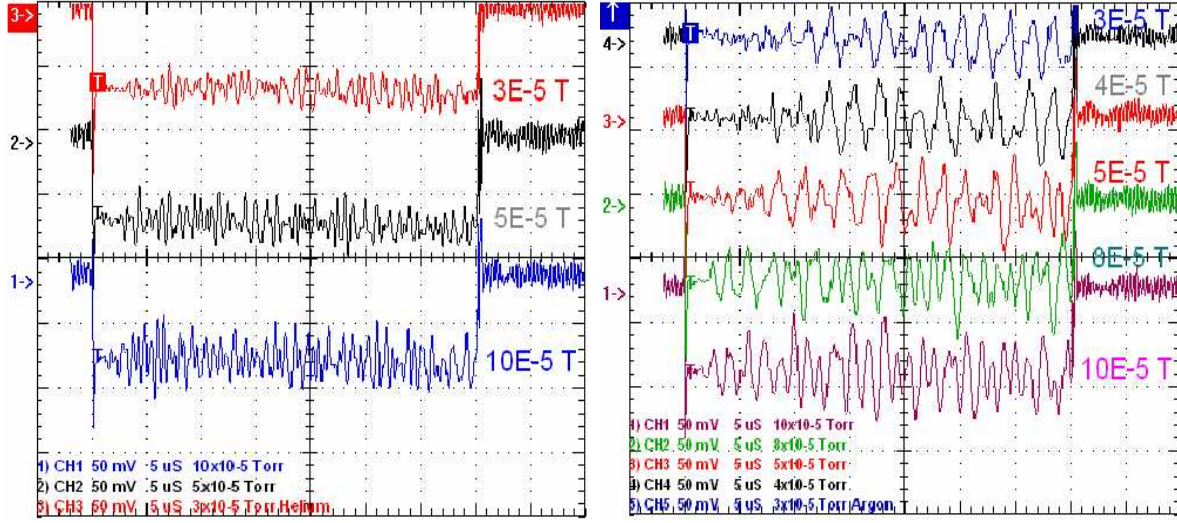


Figure 19.12: (color) Horizontal displacements of the  $35 \mu\text{s}$   $\text{H}^-$  beam in helium (left) and (right) argon gas environments at various pressures. An instability is observed and the beam displacements become saturated. The growth rate increases with gas pressure.

experiment condition satisfies this criterion. The ionization energy of the electron in the outermost shell is given by

$$U = U_0 \left( \frac{Z}{n} \right)_{\text{eff}}^2 \quad (19.104)$$

where  $Z$  is the atomic number of the gas element and  $n$  is the principal quantum number of the outermost shell of the gas atom. Here,  $U_0 = hcR_\infty = 13.605 \text{ eV}$  is Rydberg energy or the ionization energy of hydrogen,  $h = 6.582 \times 10^{-22} \text{ MeV}\cdot\text{s}$  is the Planck constant, and  $c$  is the velocity of light. Since the electrons in the inner shells shield the electric charges of the nucleus, the effective ratio  $(Z/n)_{\text{eff}}^2$  is less than the actual  $(Z/n)^2$ . The effective ratios for the various gases estimated from Eq. (19.104) are listed in Table 19.7. The velocity  $v_e$  of the electron in the outermost shell is

$$v_e = v_0 \left( \frac{Z}{n} \right)_{\text{eff}} \quad (19.105)$$

where  $v_0 = r_e c / \lambda_e = 0.0073$  is the velocity of the electron in the hydrogen atom,  $r_e = 2.818 \times 10^{-18} \text{ m}$  is the electron classical radius, and  $\lambda_e = \hbar / (m_e c) = 3.86159323 \times 10^{-13} \text{ m}$  is the reduced electron Compton wavelength. We see that the velocities of the electron in the outermost cells of the gas atoms in this experiment are roughly  $0.0073c$  to  $0.0098c$ , which are indeed much less than the velocity  $\beta c = 0.040c$  of the  $750 \text{ keV}$   $\text{H}^-$ .

Table 19.7: Ionization cross sections of various gases by 750 keV  $\text{H}^-$ . Velocities of electrons in the outermost shells of the gas atoms are estimated by an effective value of  $Z/n$  due to screening, where  $Z$  is the atomic number of the gas element and  $n$  the principal quantum number of the electron. Values of  $M^2$  and  $C$  are from experiments [27].

	H	He	N	Ar	Kr
Atomic number $Z$	1	2	7	18	36
Atomic mass number $A$	1	4	14	40	84
Ionization energy $U$ (eV)	13.6	24.6	14.5	15.6	14.0
Effective ratio $(Z/n)_{\text{eff}}^2$	1.00	1.8088	1.0662	1.1618	1.029
Electron velocity in outermost shell $v_e/c$	0.0073	0.0098	0.0075	0.0079	0.0074
Target variable in Eq. (19.106) $M^2$	0.695	0.738	3.73	4.22	6.09
Target variable in Eq. (19.106) $C$	8.115	7.056	34.84	37.93	52.38
Ionization cross section $\Sigma$ (Mb)	42.71	27.03	126.2	126.2	154.5

In the impulse approximation, the bound electrons are knocked out by a sudden transfer of energy from the incident particle. Therefore, the ionization cross section does not depend very much on the ionization energy of the target atom. From the work of Bethe [25, 26], the ionization cross section in the first Born approximation can be written as

$$\Sigma = 4\pi\chi_e^2 \left[ M^2 \left( \frac{\ln \beta^2 \gamma^2}{\beta^2} - 1 \right) + \frac{C}{\beta^2} \right], \quad (19.106)$$

where  $\beta$  and  $\gamma$  are the Lorentz factors of the incident particle with the target at rest. The two variables  $M^2$  and  $C$  depend on the generalized oscillator strength inside the target atom for all the transitions involved. Notice that this expression depends on the incident particle only through its *velocity*, which is an important consequence of the Born approximation and has been verified by many experiments [27]. The experimental values of  $M^2$  and  $C$  as well as the cross sections of the gases involved are listed in Table 19.7.

#### 19.3.4.4 Ion Bounce Frequencies

At the vacuum pressure of  $3 \times 10^{-5}$  Torr, the beam current in the transfer line is  $I \sim 56.1$  mA (see Fig. 19.10). Thus the  $\tau_b = 35 \mu\text{s}$   $\text{H}^-$  beam corresponds to a linear density of  $\lambda_b = I/(e\beta c) = 2.92 \times 10^{10} \text{ m}^{-1}$ . The  $\text{H}^-$  beam has a round cross section of radius

Table 19.8: Ion-beam resonant frequencies according to Ref. [16] for gases at various vacuum pressures or beam currents.

Gas	H	He	N	Ar	Kr
Mass number $A$	1	4	14	39	84
Resonant frequency (MHz)					
at $1 \times 10^{-5}$ Torr (61.0 mA)	1.490	0.745	0.398	0.236	0.163
at $2 \times 10^{-5}$ Torr (58.6 mA)	1.460	0.730	0.390	0.231	0.159
at $3 \times 10^{-5}$ Torr (56.1 mA)	1.429	0.715	0.382	0.226	0.156
at $4 \times 10^{-5}$ Torr (53.7 mA)	1.398	0.699	0.374	0.221	0.153
at $5 \times 10^{-5}$ Torr (51.2 mA)	1.366	0.683	0.365	0.216	0.149
at $6 \times 10^{-5}$ Torr (48.8 mA)	1.333	0.666	0.356	0.211	0.145
at $7 \times 10^{-5}$ Torr (46.3 mA)	1.299	0.649	0.347	0.205	0.142
at $8 \times 10^{-5}$ Torr (43.9 mA)	1.264	0.632	0.338	0.200	0.138
at $9 \times 10^{-5}$ Torr (41.4 mA)	1.228	0.614	0.328	0.194	0.134
at $1 \times 10^{-4}$ Torr (39.0 mA)	1.192	0.596	0.319	0.188	0.130

$a_h = a_v = 1.0$  cm. This gives the resonant frequency of  $\omega_i/(2\pi) = 1.43/\sqrt{A}$  MHz as tabulated in Table 19.8.

The resonant frequencies computed in Table 19.8 are in the neighborhood of 1 MHz, in qualitative agreement with the experimental resonant frequencies depicted in, for example, Figs. 19.11 and 19.13. The observed resonant peaks in general have wide spreads. This may be because of the nonuniformity of the linear distribution of the  $H^-$  beam as well as the variation of its transverse radius. On the other hand, there are also disagreements with theory. Definitely, we do not see the  $A^{-1/2}$  dependency given by Eq. (19.62). However, in computing the resonant frequencies in Table 19.8, we have assumed only singly charged ions. Because the velocity of the incident  $H^-$  are much greater than those of the electrons in the outermost shells of the various gases, the ionization cross sections do not depend much on the ionization energy. There are, for example, 6 electrons in the outermost shell of an argon atom or krypton atom, it will be as easy for two or more electrons to be knocked off as for one. If there were doubly or triply charged ions produced, the resonant frequency would have been  $\sqrt{2}$  and  $\sqrt{3}$  times larger. It is very plausible that the deviation of the  $A^{-1/2}$  dependency for argon and krypton is due to the production of multi-charged ions. The expression, Eq. (19.62), is independent of the gas pressure. The slight decrease of the resonant frequency with

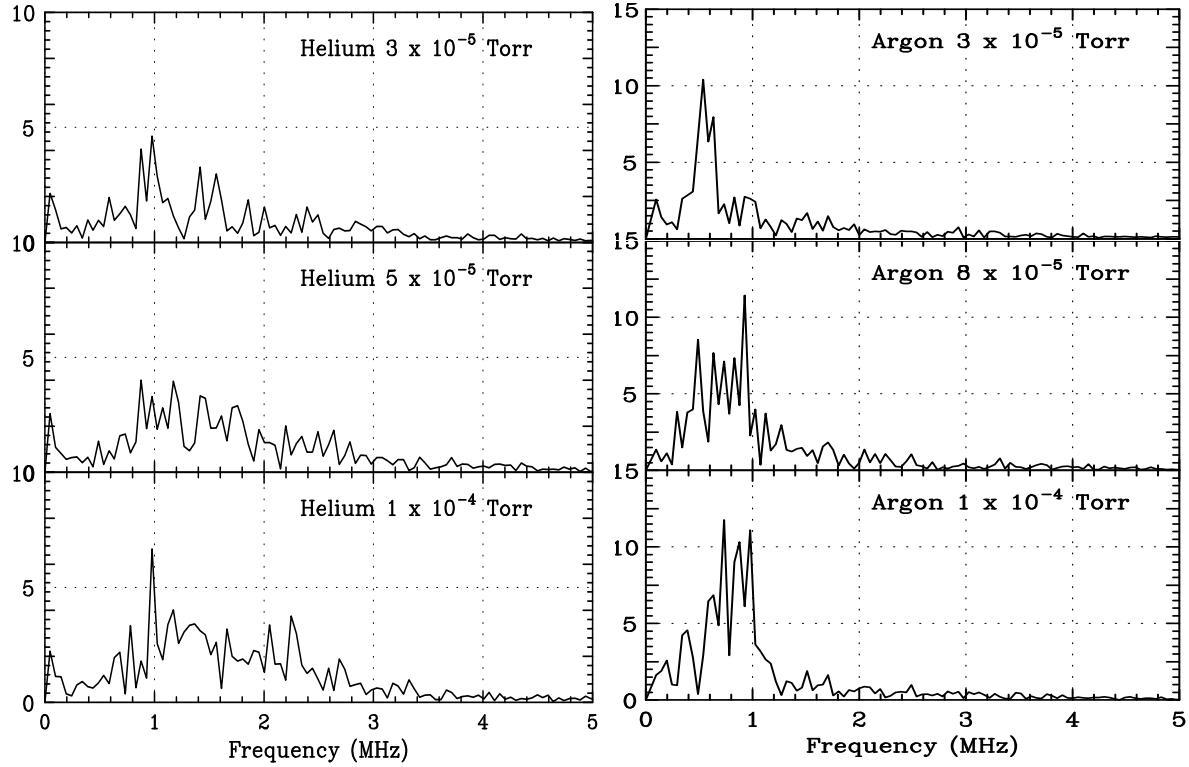


Figure 19.13: FFT of  $H^-$  beam horizontal displacement averaged over many beam pulses. The gas environments are helium (left) and argon (right). The frequency spread does not depend much on gas pressure for helium, but does depend on pressure for argon.

rising pressure tabulated in Table 19.8 is just a reflection of the  $H^-$  current or linear density as a result of possible stripping by the gas particles.

In summary, we find that the resonant frequency is not sensitive to pressure for light gases like helium and nitrogen. However, for the heavier gases such as argon and krypton, the resonant peaks are broadened and move towards higher frequencies when the pressure is larger than  $\sim 5 \times 10^{-5}$  Torr. To conclude, we plot the spreads of the experimental resonant frequencies of the different gases for all the pressures studied in Fig. 19.14. On the same plot we also include the resonant frequencies computed in Table 19.8 from  $1 \times 10^{-5}$  Torr (top trace) to  $1 \times 10^{-4}$  Torr (bottom trace). From the figure, it is evident that the theoretical predictions, as a whole, underestimate the experimental results.

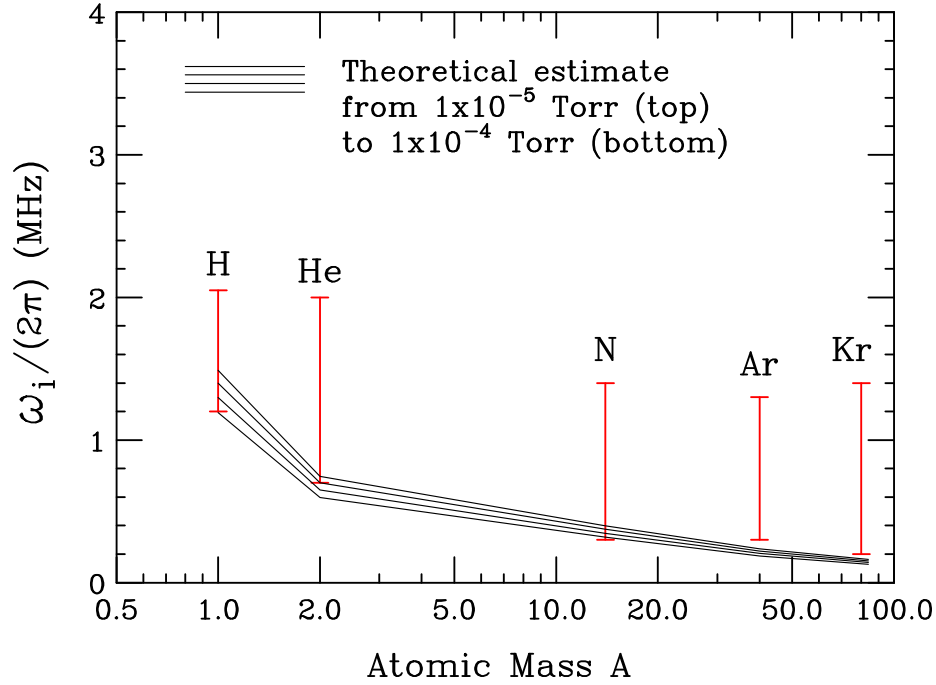


Figure 19.14: Spreads of measured resonant frequencies of different gases at all the pressures studied. The theoretical predictions from  $1 \times 10^{-5}$  Torr (top trace) to  $1 \times 10^{-4}$  Torr (bottom trace) are also shown.

#### 19.3.4.5 Growth Times

The transverse displacement of the  $H^-$  beam was measured by the BPM after Tank 2 in the linac. The excitation of transverse oscillation had been going on in the  $\ell_t \sim 10$  m of the 750 keV transfer line from the chopper to the big ion pump near the entrance into the linac. Thus the time for which the beam can actually generate and interact with the ions is  $t \sim \ell_t / (\beta c) = 0.835 \mu s$ . The growth time along the beam  $\tau_0$  in Eq. (19.89) should be derived and compared with theory. These growth times along the beam,  $\tau_0$ , at the pressure of  $1 \times 10^{-5}$  Torr are listed in the last row of Table 19.9.

Table 19.9: Computation of growth time along the  $H^-$  beam at  $1 \times 10^{-5}$  Torr. The growth time at other pressure  $p$  scales with  $p^{-1/2}$ .

	H	He	N	Ar	Kr
$\omega_b$ (MHz)	10.1	8.00	20.2	17.3	19.1
Growth time along beam $\tau_0$ ( $\mu s$ )	0.91	1.61	0.87	1.33	1.44

### 19.3.4.6 Comments

The beam-ion environment here is very different from that in an electron ring. Some relevant quantities are listed in Table 19.10. We see a huge difference:

Table 19.10: Comparison of some beam and ion parameters in a typical electron ring and in the Fermilab linac, assuming that CO is the residual gas.

	Electron Ring	Fermilab Linac Experiment
Number per bunch $N_b$	$10^{11}$	$1.3 \times 10^{13}$
Bunch length $\ell_b$	0.010	419 m
Beam radius	0.001	0.010 m
Beam linear density $\lambda_b$	$10^{13}$	$3.2 \times 10^{10}$ m <sup>-1</sup>
Residual gas pressure	$10^{-9}$	$1 \times 10^{-5}$ Torr
Gas-in-beam linear density $\lambda_{\text{gas}}$	$1 \times 10^8$	$1.0 \times 10^{14}$ m <sup>-1</sup>
Ionization cross section for CO $\Sigma$	2	133 Mb
Maximum ion linear density $\lambda_i$	640	$5.7 \times 10^{10}$ m <sup>-1</sup>
CO <sup>+</sup> ion bounce frequency $\omega_i/(2\pi)$	64	0.40 MHz
Beam bounce frequency <sup>†</sup> $\omega_b/(2\pi)$	0.00092	2.82 MHz

<sup>†</sup>10 GeV electrons are assumed for electron ring.

$\omega_b$  is the same as  $\omega_e$  referenced earlier in Eq. (19.69).

1. The ion bounce frequency in an electron ring is very much larger because of much higher electron linear density and the much smaller transverse electron beam size.
2. There are very much more ions produced in the Fermilab linac than in an electron ring. The ion linear density in an electron ring is negligibly small compared with the beam linear density, while in the Fermilab linac the ion linear density is of the same order as the beam linear density. This is due to the much higher residual gas pressure and larger ionization cross section in the transfer line where the H<sup>-</sup> are traveling with a small velocity. As a result, the beam bounce frequency in the ions becomes very much smaller in an electron ring.
3. There are 3 frequencies in the fast beam-ion instability theory, the ion bounce frequency  $\omega_i/(2\pi)$ , the beam bounce frequency  $\omega_b/(2\pi)$  [same as  $\omega_e$  referenced

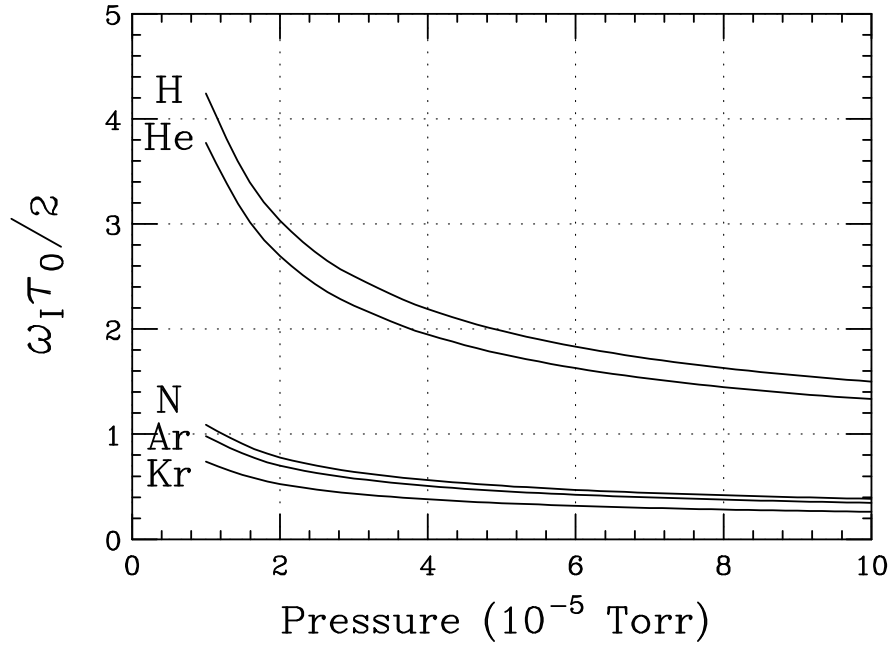


Figure 19.15: Plot of  $\frac{1}{2}\omega_I\tau_0$  versus gas pressure for various gases. When  $\frac{1}{2}\omega_I\tau_0 \gg 1$ , the neglect of the first term inside the square brackets of Eq. (19.82) is justified leading to the exponential asymptotic solution of Eq. (19.87). Since the requirement is not satisfied for nitrogen, argon, and krypton, the concept of the growth time given by Eq. (19.89) may not be correct.

earlier in Eq. (19.69)], and the betatron frequency  $\omega_\beta/(2\pi)$ . For the two situations,

$$\begin{array}{ll} \text{Electron ring} & \omega_I \gg \omega_\beta \gg \omega_b \\ \text{Fermilab linac} & \omega_b \gtrsim \omega_\beta \gtrsim \omega_I . \end{array} \quad (19.107)$$

Now let us examine whether the above approximation can be made in our situation. When we are talking about growth time, we are looking in the asymptotic behavior, like Eq. (19.4), or when  $\eta \gg 1$ , which is well satisfied when we are considering a position along the beam which is a few growth times behind the head. The neglect of the first term in the square brackets therefore requires the satisfaction of

$$\frac{\omega_I\tau_0}{2} \gg 1 . \quad (19.108)$$

In Fig. 19.15, we plot  $\frac{1}{2}\omega_I\tau_0$  as a function of pressure for the different gases. It is clear that criterion in Eq. (19.95) is satisfied for hydrogen and helium when the pressure is

low and becomes marginal when the pressure is higher than  $5 \times 10^{-5}$  Torr. For nitrogen, argon, and krypton, the criterion fails. This implies that the concept of a growth time  $\tau_0$  given by Eq. (19.89) may not be valid for these heavier gases. Therefore, we cannot say whether the results for nitrogen, argon, and krypton agree with the linear theory of fast beam-ion instability or not. A more sophisticated solution of Eqs. (19.76) and (19.77) must be obtained without the deletion of the first term in the square brackets before further comparison with experiment can be made for these heavier gases. Even the approximation of neglecting the second derivatives in obtaining Eqs. (19.76) and (19.77) should be re-examined.

Even for hydrogen and helium, the resonant frequency is around 1 MHz and less, and the passage time through the 10 m transfer line is  $0.835 \mu\text{s}$ . This implies that the beam and the ion made less than one oscillation about each other. It is hard to visualize how a coherent instability can be established within such a short time. This is another reason why we are skeptical whether the expression for growth time could be applied to this experiment.



## 19.4 Exercises

- 19.1. Modify the coupled proton and electron equations of motion [Eqs. (19.9) and (19.10)] by including the influence of an infinitely conducting cylindrical beam pipe of radius  $b$ . Without taking into account the distributions of the various tunes, solve the equations for the threshold of coupled-centroid instability [similar to Eq. (19.17)] and the initial growth rate [similar to Eqs. (19.17) and (19.18)].
- 19.2. Derive in detail Eq. (19.59) for the kinetic energy of an electron hitting the wall of the beam pipe after it grazes the opposite wall.
- 19.3. In the experiment for measuring coupled-centroid instability at the Los Alamos PSR, the bunch occupies 2/3 of the circumference of the storage ring. The coherent frequency which is close to the electron bounce frequency at CD 1 or 6.1  $\mu\text{C}$  is shown in Fig. 19.5. Other information of the PSR are listed in Table 19.1.
  - (1) Assuming a parabolic linear distribution of the proton bunch, and the maximum coherent or bounce frequency of 240 MHz, estimate the transverse size of the proton beam.
  - (2) From the peak value of the bounce frequency, estimate the location along the proton beam where the electron density is at a maximum.
- 19.4. Fermilab is proposing a new high intensity booster having circumference 711.304 m with rf harmonic 4. Protons are injected at the kinetic energy of 400 MeV to an intensity of  $8.6 \times 10^{12}$  per bunch. At the end of injection, each proton bunch has a uniform linear density but is occupying 2/3 of the rf bucket. The transverse cross section of the beam is circular with a radius of 2.35 cm.
  - (1) Assuming the bunch gap is totally clean, show that electrons will not be trapped inside the proton beam.
  - (2) If a fraction  $\eta$  of protons is spilled into the bunch gaps, compute the minimum  $\eta$  that will lead to electron trapping.
- 19.5. Starting from the equations of coupled transverse motion, Eqs (19.9) and (19.10), assuming circular distributions for the protons and electrons, derive the Laslett-Sessler-Möhl stability criterion, Eq. (19.46).
- 19.6. In Tables 19.5 and 19.6, rows 1-6, 9-12, and 16 are inputs. Compute the output rows 7-8 and 13-15.



# Bibliography

- [1] H. Gruner, G. Lambertson, Proc. VIII Int. Conf. on High Energy Accel., p.308 (1971).
- [2] H.G. Hereward, CERN Report CERN-71-15, (1971).
- [3] R. Macek, *Overview of New Developments on the PSR Instability*, Proceedings of 8th Advanced Beam Dynamics Mini-Workshop on Two-Stream Instabilities in Particle Accelerators and Storage Rings, Santa Fe, Feb. 16-18, 2000, web site: <http://www.aps.anl.gov/conferences/icfa/proceedings.html>.
- [4] M. Blaskiewicz, *The Fast Loss Electron Proton Instability*, Proceedings of the Workshop on Instabilities of High Intensity Hadron Beams in Rings, ed. T. Roser and S.Y. Zhang, Upton, N.Y., 1999, p. 321; *Estimating Electron Proton Instability Thresholds*, Proceedings of 8th Advanced Beam Dynamics Mini-Workshop on Two-Stream Instabilities in Particle Accelerators and Storage Rings, Santa Fe, Feb. 16-18, 2000, web site: <http://www.aps.anl.gov/conferences/icfa/proceedings.html>.
- [5] J. Rosenzweig and P. Zhou, *Coherent Beam-ion Instabilities in the Fermilab Antiproton Accumulator, Ion Trapping in the Tevatron with Separated Orbits, Ion Clearing Using Cyclotron Shaking*, Proceedings of Fermilab III Instabilities Workshop, Fermilab, Batavia, Ed. S. Peggs and M. Harvey, June 25-29, 1990, p. 9, 26, and 39.
- [6] K. Harkay, *Electron Cloud Effects at APS*, Proceedings of 8th Advanced Beam Dynamics Mini-Workshop on Two-Stream Instabilities in Particle Accelerators and Storage Rings, Santa Fe, Feb. 16-18, 2000, web site: <http://www.aps.anl.gov/conferences/icfa/proceedings.html>.
- [7] D. Neuffer, E. Colton, D. Fitzgerald, T. Hardek, R. Hutson, R. Macek, M. Plum, H. Thiessen, and T.-S.Wang, Nucl. Instr. Meth. **A321**, 1 (1992).

- 
- [8] In the reference below, aluminum pipe with titanium coating is mentioned: <http://www.ornl.gov/~nsns/CDRDocuments/CDRSections/CDRSections.html>. In the more recent design, however, stainless steel beam pipe with TiN coating is used.
- [9] Obtainable by contour integration or see for example, I.S. Gradshteyn and I.M. Ryzhik, *Table of Integrals, Series, and Products*, Academic Press, Inc., Formula 3.644-4.
- [10] A. Ruggiero and M. Blaskiewicz, *e-p Instabilities in the NSNS Accumulator Ring*, Proceedings of the 1999 Particle Accelerator Conference, New York, 1999, p.1581.
- [11] M. Blaskiewicz, *Instabilities in the SNS*, Proceedings of the 1999 Particle Accelerator Conference, New York, 1999, p.1611.
- [12] W. Schnell and B. Zotter, CERN Report ISR-GS-RF/76-26 (1976).
- [13] L.J. Laslett, A.M. Sessler and D. Möhl, Nucl. Inst. Meth. **121** 517 (1974).
- [14] Tai-Sen F. Wang, *A Theoretical Study of Electron-Proton Instability I and II*, LANL Report PSR-96-004 and PSR-96-004 (1996).
- [15] R. Macek, talk given at the 8th Advanced Beam Dynamics Mini-Workshop on Two-Stream Instabilities in Particle Accelerators and Storage Rings, Santa Fe, New Mexico, February 16-18, 2000
- [16] T.O. Raubenheimer and F. Zimmermann, Phys. Rev. **E52**, 5487 (1995).
- [17] A.W. Chao, *Lecture Notes on Topics in Accelerator Physics*, US Particle Accelerator School, 5-16 June 2000, SUNY Stony Brook, New York, available at <http://www.slac.stanford.edu/~achao/lecturenotes.html>.
- [18] J. Byrd *et al.*, Phys. Rev. Lett. **79**, 79 (1997).
- [19] H. Fukuma *et al.*, (unpublished).
- [20] M. Kwon *et al.*, Phys. Rev. **E57**, 6016 (1998).
- [21] E. McCrory, G. Lee, and R. Webber, *Observation of Transverse Instabilities in FNAL 200 MeV Linac*, Proceedings of 1988 Int. Linac Conf. 3-7 October 1988, Williamsburg, VA.

- 
- [22] I.A. Soloshenko, *Space Charge Compensation and Collective Processes in the Intensive Beams of  $H^-$  Ions*, AIP Conf. Proceedings **380**, 1995, pp 345.
  - [23] M.D. Gabovich, V.P. Goretsky, D.G. Dhabbarov, and A.P. Naïda, Institute of Physics of Ukrainian Science Academy **N 9**, Kiev, 1979, pp 18.
  - [24] M. Popovic and T. Sullivan, *Observation of a  $H^-$  Beam Ion Instability*, Proceedings of XX Int. Linac Conf. 21-25 August 2000, Monterey, CA.
  - [25] H. Bethe, Ann. Physik **5**, 325 (1930).
  - [26] M. Inokuti, Rev. Mod. Phys. **43**, 297 (1971).
  - [27] F.F. Rieke and W. Prepejczal, Phys. Rev. **A6**, 1507 (1972).

